J. Fluid Mech. (2008), *vol.* 607, *pp.* 351–386. © 2008 Cambridge University Press
doi:10.1017/S0022112008002188 Printed in the United Kingdom

Asymmetry and transition to turbulence in a smooth axisymmetric constriction

J. VÉTEL, A. GARON, D. PELLETIER AND M.-I. FARINAS

Department of Mechanical Engineering, École Polytechnique de Montréal, C.P. 6079, Succursale Centre-ville, Montréal, Québec, H3C 3A7, Canada

(Received 18 May 2007 and in revised form 22 April 2008)

The flow through a smooth axisymmetric constriction (a stenosis in medical applications) of 75 % restriction in area is measured using stereoscopic and time-resolved particle image velocimetry (PIV) in the Reynolds number range $Re \sim 100$–1100. At low Reynolds numbers, steady flow results reveal an asymmetry of the flow downstream of the constriction. The jet emanating from the throat of the nozzle is deflected towards the wall causing the formation of a one-sided recirculation region. The asymmetry results from a Coanda-type wall attachment already observed in symmetric planar sudden expansion flows. When the Reynolds number is increased above the critical value of 400, the separation surface cannot remain attached and an unsteady flow regime begins. Low-frequency axial oscillations of the reattachment point are observed along with a slow swirling motion of the jet. The phenomenon is linked to a periodic discharge of the unstable recirculation region inducing alternating laminar and turbulent flow phases. The resulting flow is highly non-stationary and intermittent. Discrete wavelet transforms are used to discriminate between the large-scale motions of the mean flow and the vortical and turbulent fluctuations. Continuous wavelet transforms reveal the spectral structure of flow disturbances. Temporal measurements of the three velocity components in cross-sections are used with the Taylor hypothesis to qualitatively reconstruct the three-dimensional velocity vector fields, which are validated by comparing with two-dimensional PIV measurements in meridional planes. Visualizations of isosurfaces of the swirling strength criterion allow the identification of the topology of the vortices and highlight the formation and evolution of hairpin-like vortex structures in the flow. Finally, with further increase of the Reynolds number, the flow exhibits less intermittency and becomes stationary for $Re \sim 900$. Linear stochastic estimation identifies the predominance of vortex rings downstream of the stenosis before breakdown to turbulence.

1. Introduction

A stenosis is a medical term referring to a constricted segment in an artery. Atherosclerotic plaque develops on the arterial wall and forms local deposits, inducing clinically significative health risks when the blockage is greater than about 70 % of the cross-section area. A partial or total circulatory occlusion in a coronary artery reduces the blood supply to the heart and significantly increases myocardial infarction (heart attack) probabilities. In the carotid artery this can lead to brain damage (cerebral vascular accident). The link between fluid mechanics in the poststenotic blood flow and the progression of atherosclerosis has been known for a long time, but most of the initial studies were primarily concerned with flow resistance and did not exploit

https://doi.org/10.1017/S0022112008002188 Published online by Cambridge University Press

similarity rules. These articles were mostly published in medical journals. Analysis of stenotic flows expanded in scope and numbers in the early 1970s with an increase of published works on *in vitro* measurements in mechanics and biomechanics journals. These laboratory models used a blood analogue, such as water–glycerin mixtures, as the working fluid. In most cases the experimental loop used a smooth occlusion (sinusoidal axial profile) to represent the stenosis. Test sections of different length, and area reduction, were inserted in an optically clear rigid pipe. The inlet flow rate was either steady or defined by a pulsatile function, ranging from simple oscillations to more complex waveforms to reproduce the physiological cardiac cycle (recent reviews of the general characteristics of blood flow in arteries can be found in Ku 1997; Berger & Jou 2000).

Pulsatile flows differ from steady flows in many respects and particularly transition to turbulence, so that previous studies have rapidly focused on physiological regimes. However, during the last decade, we have observed a steady increase of end-of-stage heart failure treatments through implantations of continuous blood pump ventricular assist devices. This has revived interest in steady or quasi-steady flow experiments. These pumps are now designed as a bridge to transplant, as a bridge to recovery or as destination therapy. When they are used at their most-efficient point, the aortic valve is closed and the flow rate within the systemic circulation is constant. It is this latter situation which is relevant to this study.

Early fluid mechanics studies originally focused on predictions or measurement of pressure distribution along stenoses, of wall shear-stress, of velocity distribution, of flow separation and of turbulence (Young 1979). Forrester & Young (1970*a*, *b*) analysed the steady flow of an incompressible fluid in an axisymmetric converging–diverging tube. Their experiments showed that flow separation occurs even in mild stenoses and that they are only small differences between blood and water. The problem of pressure drop across the constriction was investigated in laminar and turbulent flow (Young & Tsai 1973; Clark 1976*a*). Young & Tsai (1973) described in detail flow characteristics in models of axisymmetric and non-symmetric arterial stenoses and in particular used hot-film probes to detect transition to turbulence. Mean turbulent flow fields were investigated by Clark (1976*b*) with hot-film anemometry and by Deshpande & Giddens (1980) with a laser Doppler anemometer, leading also to the determination of fluctuating velocity spectra (Kim & Corcoran 1974). The nature of poststenotic disturbances was also analysed by coupling frequency spectra with flow visualizations to identify vortex shedding in the separated shear layer (Cassanova & Giddens 1978; Ahmed & Giddens 1983*a*, *b*).

In general, the investigations previously described were able to provide pressure losses across constrictions based on empirical dimensional analysis and the length of recirculation region for very mild stenoses. However, flow models failed to reproduce flow characteristics for more severe constrictions. For these reasons, computational fluid mechanics played an important role in flow predictions. Lee & Fung (1970) performed numerical simulations of the Navier–Stokes equations in circular cylindrical tubes with a local Gaussian-shaped constriction. The steady flow was calculated for Reynolds numbers Re up to 25 (based on the flow conditions in the unoccluded pipe), and separation was observed to begin at a value of 10. Using steady equations in cylindrical form, Deshpande, Giddens & Mabon (1976) presented solutions at Reynolds numbers sufficiently large to ensure that the full range of laminar flow was covered. Validation of the numerical procedure was obtained by comparisons with available experimental data in the case of sinusoidal stenoses. More recently, Bluestein *et al.* (1999) used the $k-\omega$ model to describe unsteady vortex

https://doi.org/10.1017/S0022112008002188 Published online by Cambridge University Press

shedding formation in the separated flow region of a smooth stenosis. However, conventional turbulence models fail to correctly predict transitional arterial flows (Varghese & Frankel 2003), and a full three-dimensional time-dependent calculation seems necessary to predict the complex unsteady and turbulent flow behaviour. To date, only two studies have treated such calculations in the case of steady inlet flow conditions. Sherwin & Blackburn (2005) applied linear stability analysis and direct numerical simulation (DNS) to examine the development of three-dimensional instabilities in flows through a sinusoidal stenosis. A Coanda-type wall attachment and transition to turbulence were found to occur at a critical Reynolds number of 722. Since the bifurcation was subcritical, the hysteresis behaviour allowed asymmetry to be maintained in simulations down to $Re = 688$. More recently, Varghese, Frankel & Fischer (2007) studied the influence of a geometric perturbation, in the form of a stenosis eccentricity, on the poststenotic flow. Results indicated a breaking of the symmetry downstream of the stenosis causing the jet to deflect towards the side of the eccentricity.

In the simulation of Varghese *et al.* (2007), the geometric perturbation was responsible for transition to turbulence, whereas in the work of Sherwin & Blackburn (2005), a small perturbation flow component derived from the leading instability mode was added in the numerical simulation to an unstable base flow, then the flow was evolved to saturation. Comparisons with previous experimental studies are unfortunately limited since critical Reynolds numbers have not been investigated. Moreover, most of the time, comparisons are essentially qualitative. Cassanova & Giddens (1978) used visualization and velocity spectra computed with hot-wire signals to describe the flow at $Re = 635$ whereas the inflow velocity profile, inconsistent with fully developed flow, was not given. Velocity spectra are also available in Ahmed & Giddens (1983*b*) but for only two Reynolds numbers, $Re = 500$ and 1000. Taken as a whole, previous experimental studies seem to indicate that discrete frequency oscillations occurred at $Re = 500$ and 635, more consistent with shear-layer oscillation rather than developed turbulence, but disagree with numerical predictions. According to Sherwin & Blackburn (2005), these oscillations were potentially triggered by upstream noise. Ahmed & Giddens (1983*a*) also used laser Doppler anemometry to describe mean flow properties. Varghese *et al.* (2007) compared these data with their numerical simulation and showed a good agreement only immediately downstream of the stenosis. However, for an axisymmetric stenosis, i.e. for the same geometry as used by Sherwin & Blackburn (2005), and in the absence of non-axisymmetric perturbation, the DNS described by Varghese *et al.* (2007) produced laminar flow for Reynolds numbers of 500 and 1000 with no evidence of shear-layer oscillation. Thus, since they compared numerical results with experimental data obtained from averaging unsteady velocity fluctuations totally absent in the simulations, these discrepancies are not surprising.

Comparatively more experimental details are available in axisymmetric abrupt expansion flows. Even if the geometry differs from a smooth expansion, one would expect the presence of similar phenomena. Monnet, Menard & Sigli (1982) studied the flow through a cylindrical duct in the vicinity of a section discontinuity for very small Reynolds numbers. The evolution of the stationary vortex cell was analysed using visualization techniques. Macagno & Hung (1967) investigated the laminar flow regime in a conduit expansion by comparing steady flow visualizations with finite difference methods for a Reynolds number range up to 200. Iribarne *et al.* (1972) used a non-disturbing photochromic tracer visualization technique to study the flow properties of a laminar pipe jet entering a 1:2 expansion-ratio circular tube. They

https://doi.org/10.1017/S0022112008002188 Published online by Cambridge University Press

characterized the recirculation length for flows ranging from laminar to turbulent regimes. Similar measurements were conducted by Back & Roschke (1972) with dye injection for still higher Reynolds numbers. Even if general trends appear to be similar for all studies, discrepancies in quantitative properties are clearly pointed out. In particular, unsteady effects are observed for Re values of the order of a few hundreds (based on upstream flow conditions) but differ from author to author; Feuerstein, Pike & Round (1975) reported an even higher value of 1000. The determination of the critical Reynolds number is sensitive to the experimental technique used (especially in the presence of high flow fluctuations) as it depends on the axial position of a hot-film probe or the accuracy of the characterization of the reattachment point based on visual inspection of dye. Despite these difficulties, Latornell & Pollard (1986) showed that the onset of instabilities depends on the inlet velocity profile. More generally, the upstream flow conditions, i.e. the velocity distribution and the residual turbulence intensity at the inflow section, are noise sources that trigger flow oscillations.

The cited references all report an interesting phenomenon when the Reynolds number approaches its critical value: high-intensity velocity fluctuations give rise to oscillations of the reattachment point location, making the measurement of the recirculation length difficult or impossible. Iribarne *et al.* (1972) observed that when 'the attachment point is approached, the flow becomes increasingly irregular', and in the recirculation region, the flow acquires a substantial swirling motion. The same observation was described by Latornell & Pollard (1986) as the Reynolds number corresponding to the maximum reattachment length was approached. They stated that the flow exhibits non-periodic unsteadiness inducing a fluctuation of the reattachment point location, the phenomenon being more 'frequent and violent' with further increases in Re. In addition, this unsteady pulsation produced a momentary recirculation length of $\sim$10 step heights greater than the maximum reported in their correlations based on mean values. The experiment of Sreenivasan & Strykowski (1983) provides a more remarkable example of such flow fluctuations. A hot-wire probe located on the centreline of the pipe and downstream of the sudden expansion for a Reynolds number between 1500 and 1700 registered large-scale oscillations so regular and repeatable that the time traces had the form of square signals.

All these examples show that experimental investigations in smooth or abrupt axisymmetric expansions were generally concerned with time-averaged flow properties, local velocity measurement methods (hot-wire or hot-film anemometers, laser Doppler velocimetry, wall pressure transducers) and qualitative visualization methods (usually by injection of a dye filament or hydrogen bubbles). It was usually postulated that velocity fluctuations developing downstream of constrictions were caused by vortex ring convection, even though no quantitative measurements could support this hypothesis. Few experiments addressed the problem of obtaining a description of instantaneous flow structures, from the onset of instabilities to the turbulent state. The use of PIV for example to visualize instantaneous flow patterns is very rare and when used, measurements are made in meridional planes to provide data for validation of computational fluid dynamic. Therefore, previous experimental studies assumed that the flow was two-dimensional.

The main objective of the present study is to provide detailed measurements of the flow past a smooth axisymmetric constriction with steady axisymmetric upstream flow conditions. In particular three-dimensional flow information not covered in previous experimental studies is obtained for a full range of Reynolds numbers from steady to turbulent flow. Furthermore, we attempt to relate some observations made on different models of vessel constrictions with some phenomena that also occur in sudden

https://doi.org/10.1017/S0022112008002188 Published online by Cambridge University Press

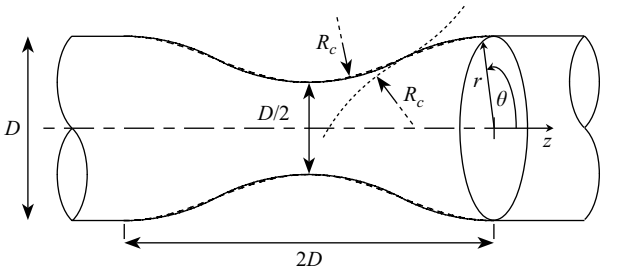

FIGURE 1. Geometrical parameters of the constriction: ——, actual stenosis with $R_c = 17D/16$; — — —, sinusoidal stenosis.

expansion flows which have not been noted previously. To this end, stereoscopic PIV and time-resolved PIV are used simultaneously to obtain velocity information in both space and time, which allows the capture of any three-dimensional perturbation. In a more general view, PIV measurements in meridional planes are found to closely match the well-known characteristic two-dimensional vortex signatures of hairpin vortex packets in wall turbulence. While the imprints of hairpin vortices in two-dimensional experimental data are usually identified with evidence, the shape of three-dimensional large-scale coherent structures can only be speculated. The present work uses the assumption of the Taylor hypothesis to reconstruct three-dimensional velocity fields with temporal data. The good agreement between the reconstructed velocity fields and the two-dimensional measurements allows three-dimensional representations of vortical structures to be obtained, leading to the unique observation of vortices of different shape belonging to the hairpin like structure family.

The flow setup and the measurement procedure are introduced in § 2, and signal processing based on wavelet transforms is developed for the case of non-stationary and transient time signals. The following sections present results in a manner reflecting the evolution of flow when the Reynolds number is progressively increased. The steady-flow properties for the smallest Reynolds numbers investigated are detailed in § 3. This is completed by a description of the development of flow instabilities in § 4. Vortex structures are visualized in § 5 using a vortex identification criterion, prior to the development of turbulence considered in § 6, which addresses in addition time-averaged quantities of the stationary flow. Additional discussions and conclusions are covered in § 7.

2. Experimental procedure

2.1. *Geometrical and flow parameters*

The axisymmetric constriction considered here, shown in figure 1, exhibits a 50 % restriction in radius (75 % restriction in area) of a circular pipe of diameter $D = 20.5$ mm. The choice in the area reduction reflects a large number of observations of vascular occlusions and is a typical value used in experimental and numerical laboratory models. The contours of the stenotic region are composed of circular arcs of the same length and radius $R_c = 17D/16$. The choice of a single curvature radius adequately represents the usual sinusoidal axial profile used in the modelling of axisymmetric stenoses, as shown in figure 1. The length of the constriction is $2D$ and is typical of values used in previous works. The cylindrical coordinate system (z, r, θ) is used to define the streamwise (axial), radial and azimuthal directions, the origin is set on the axis at the stenosis exit plane.

https://doi.org/10.1017/S0022112008002188 Published online by Cambridge University Press

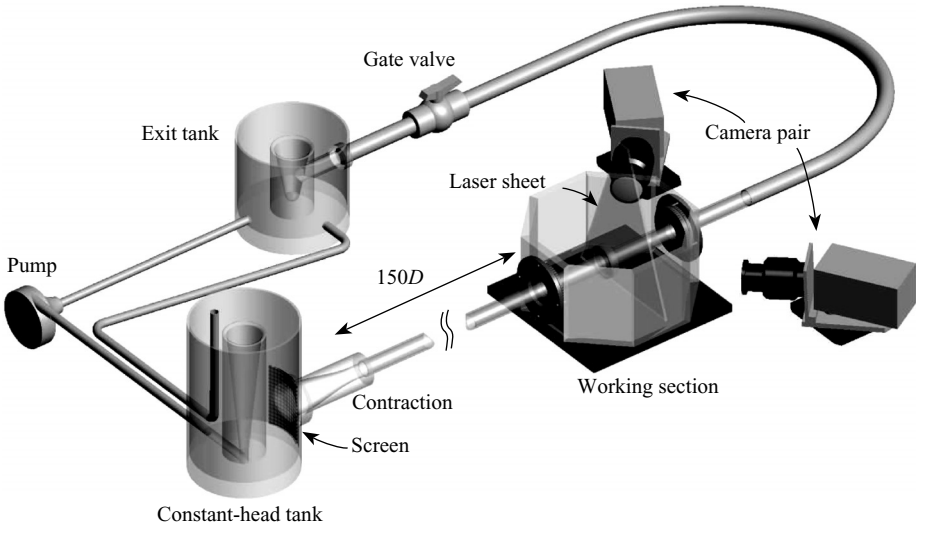

FIGURE 2. Schematic view of the experimental setup with the stereoscopic PIV arrangement.

The Reynolds number Re is defined as $u_m D/\nu$, where ν is the kinematic viscosity and u_m the sectional average velocity in the unoccluded pipe. It is the single controlling parameter of the flow generated by a constant flow rate. The working fluid is a water–glycerin mixture that allows the Reynolds number to be in the range $Re = 116$ to $Re = 1160$.

2.2. *Flow facility*

A schematic view of the setup is presented in figure 2. The flow-rig consists of a recirculating test circuit with an optically clear pipe upstream and downstream of the constriction. The driving system is provided by a constant-head tank connected to the test section through a smooth contraction. A fine screen is placed upstream of the contraction to remove bubbles from the fluid. A tube of approximately $150D$ in length is installed upstream of the stenosis to ensure that a fully developed parabolic Poiseuille profile is obtained at the inlet plane. The stenosis was fabricated on a numerically controlled five axis milling machine and polished. Its final geometry is within 25 μm of the prescribed shape. A discharged tank is placed at the exit of the pipe downstream of the stenosis to minimize unsteady perturbations. The flow then returns to the driving reservoir filled by an isolated centrifugal pump to avoid vibrations. Since the pump is also designed to be used as a blood supply, its own design dampens most of the flow perturbations. At the low mass flow rates investigated, the elevation of the constant-head tank above the exit tank is small. Thus, flow disturbances were sufficiently reduced at the pipe entrance by the screen and the contraction that no discernible effects were found when additional screens were added. This indicates that the driving system is satisfactorily free of noise. The presence of non-axial or swirl motions in the inflow was also investigated and results showed that in-plane velocity levels measured at cross-sections are below 1 % of u_m, i.e. below the measurement accuracy. The free surface of the head tank is maintained at a constant level by an overflow return into the exit tank. The flow is controlled by a gate valve and an accurate measurement of the flow-rate is achieved by an electromagnetic flow-meter.

https://doi.org/10.1017/S0022112008002188 Published online by Cambridge University Press

PIV is used to measure the two components of the instantaneous velocity vector in longitudinal-radial planes, as well as the three components of the instantaneous velocity vector in cross-section planes. For these latter measurements, stereoscopy is employed to obtain the two in-plane and the out-of-plane components of the displacement vector, from which the full velocity vector is recovered using a calibration procedure (Prasad 2000). The main specification in the design of the flow rig was to allow stereoscopic PIV measurements in different planes normal to the axis and to extract velocity data from a single calibration set. The choice was to keep the laser-light sheet and the two cameras fixed, and to move the working section (the optical arrangement is illustrated in figure 2). The stenosis is placed between two connected transparent pipes supported by rings specially built to allow the translation of the working section in the pipe-axis direction as well as its rotation about the centreline, and ensuring appropriate watertightness. The test section is placed in an octagonal tank filled with pure glycerin, allowing two-dimensional PIV measurements in any meridional plane as well as three-dimensional measurements in any axis-normal plane. The calibration parameters were computed at a given cross-section of the pipe axis and were assumed to hold throughout the length of the pipe. This assumption was later verified by comparing the measured velocities at different positions along the pipe axis (see below). The agreement was excellent thanks to accurate machining and polishing of the acrylic tubes whose tolerance did not exceed $\pm 25\,\mu$m.

The working fluid is seeded with fluorescent tracer particles (Rhodamin B) with a mean diameter $d_p \sim 10\,\mu$m, which allows the use of an optical bandpass filter in front of the lens to remove direct reflections of laser light. The flow is illuminated with a cw-diode pumped Q-switched double Nd:YAG laser, suitable for generation of short pulses at high repetition rates. Two high-speed CCD cameras (Dantec Dynamics Nanosense TR camera) are synchronized with the laser pulses to run at frame rates up to 400 Hz. The treatment used for cross-correlation estimation is performed with the Dantec Dynamics software. An adaptive multipass correlation in 32×32 pixel interrogation windows is used with an overlap of 50 %. The vectors with a signal-to-noise ratio below 1.2 are removed and replaced with the median filter.

Inflow conditions, i.e. upstream of the stenosis, are given in figure 3(*a*) which shows the three-dimensional profile of the normalized streamwise velocity for a Reynolds number of 928 at the inlet $z/D = -3$ (a zero velocity is added at $r/D = 0.5$). It is clear that the inlet velocity profile is axisymmetric, and that the maximum velocity of $2.02u_m$ is close to the theoretical value of 2 for Poiseuille flow. Similar measurements were carefully conducted for each Reynolds number (figure 3*b*) and the flow remained axisymmetric to within the experimental error. Therefore, the inlet velocity profile can be examined in an arbitrary meridional plane as shown in dimensional form in figure 3(*c*) for values of the Reynolds number that are multiples of $\Delta Re = 116$. The inlet velocity profile measured with two-dimensional PIV measurements at $Re = 928$ is also traced together with the Poiseuille profile. We conclude that the flow upstream of the stenosis has the fully developed parabolic profile for the Reynolds number range investigated. Measurements at the inlet section showed velocity fluctuation levels less than 1 % of u_m, which is estimated to be the order of the background noise of the PIV system. This suggests that the inflow turbulence intensity was below the level of 1 %.

These results were also used to estimate the accuracy of the PIV measurements. The inlet velocity profiles were obtained at $z/D = -3$ whereas the calibration was performed on measurements at $z/D = 1$. The uncertainty was calculated from the standard deviation of the streamwise velocity profiles at the inlet location from the

https://doi.org/10.1017/S0022112008002188 Published online by Cambridge University Press

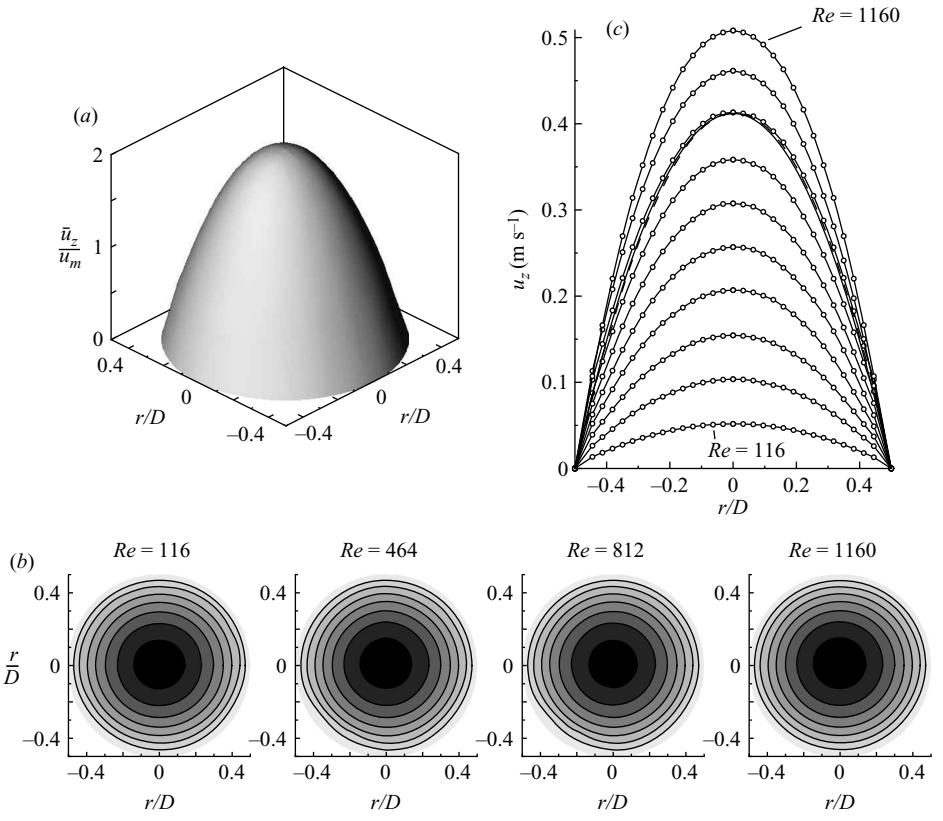

FIGURE 3. Inlet velocity profiles obtained at $z/D = -3$ from the stereoscopic measurements. (a) Three-dimensional view for $Re = 928$. (b) Contours of streamwise velocity for different Reynolds numbers. (c) Sectional profiles from $Re = 116$ to $Re = 1160$ with an increment $\Delta Re = 116$; – – –, data obtained with two-dimensional PIV for $Re = 928$; ——, standard parabolic Poiseuille profile for $Re = 928$.

parabolic profile. The error (including the inherent PIV procedure, the machining defaults and the position misalignments) was estimated to be less than 4 % when normalized by the average velocity u_m.

2.3. *Data processing*

The continuous wavelet transform is used to analyse non-stationary data and velocity signals with different time scales. The wavelet transform of a signal $f(t)$ at time u and scale s is given by

$$Wf(u, s) = \langle f, \psi_{u,s} \rangle = \int_{-\infty}^{+\infty} f(t) \frac{1}{\sqrt{s}} \psi^* \left(\frac{t-u}{s} \right) \mathrm{d}t,$$

where $\psi(t)$ is the mother wavelet. This projection of a signal on a family of time–frequency atoms, representing bandpass filters, allows a time–frequency representation of the signal. A characteristic frequency f_c of the mother wavelet can be used instead of the scale s to relate the frequency spectra of the Fourier transforms to those of the

https://doi.org/10.1017/S0022112008002188 Published online by Cambridge University Press

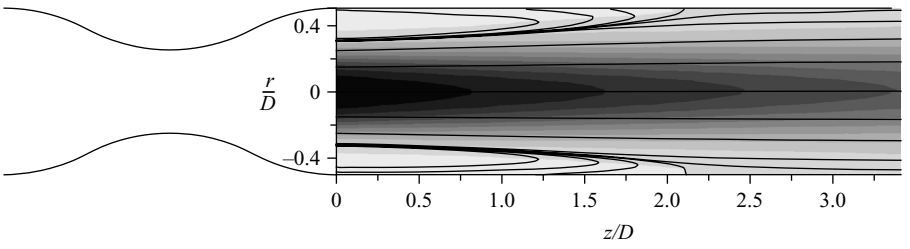

FIGURE 4. Streamlines superimposed on contours of mean streamwise velocity for $Re = 116$. Darker regions correspond to high velocity levels.

wavelet transforms. Usually, the bandpass centre of the energy spectrum

$$f_c = \left(\frac{\int_0^{+\infty} f^2 |\hat{\psi}(f)|^2 \, \mathrm{d}f}{\int_0^{+\infty} |\hat{\psi}(f)|^2 \, \mathrm{d}f} \right)^{1/2},$$

where $\hat{\psi}(f)$ is the Fourier transform of $\psi(t)$, is used. Therefore, for a scaled wavelet, the passband frequency is simply given by $f = f_c/s$. All the results presented here have been obtained with the Morlet wavelet, the most commonly used complex wavelet, for its efficiency at resolving the frequency distribution of multi-scale signals (Farge 1992).

In the case of a discrete wavelet transform, discrete values of the dilation and translation parameters, u and s, are used. Using the dyadic grid, it is possible to reconstruct a zero average signal $f(t)$ with the inverse discrete wavelet transform. In the case of finite discrete input data, a signal can be expressed as a combination of an approximation signal at arbitrary scale index m_0 added to a succession of signal details from scale m_0 down to $m = 1$. Hence, the original signal can be written as

$$f(t) = f_{m_0}(t) + \sum_{m=1}^{m_0-1} d_m(t).$$

where f_{m_0} and d_m represent the approximation at scale 2^{m_0} and the detail variations at the scale 2^m, respectively. This form was used in this study with each component u_i of the velocity vector to separate the fluctuating part u_i' from the time-varying mean velocity $\tilde{u}_i(t)$:

$$u_i(t) = \tilde{u}_i(t) + u_i'(t),$$

with

$$\tilde{u}_i(t) = \bar{u}_i + u_{i_{m_0}}(t),$$

where $\bar{u}_i$ denotes the time-average of $u_i(t)$. The discrete wavelet transform appears simply as a filter to separate velocity fields into larger and smaller time scales than a characteristic scale associated with m_0. We use the Daubechies compactly supported wavelet with 20 vanishing moments because the wavelet basis leads to a good frequency localization.

3. Steady-flow observations

The main flow characteristics are illustrated in figure 4 with time-averaged velocity levels obtained in a meridional plane from two-dimensional measurements. The

https://doi.org/10.1017/S0022112008002188 Published online by Cambridge University Press

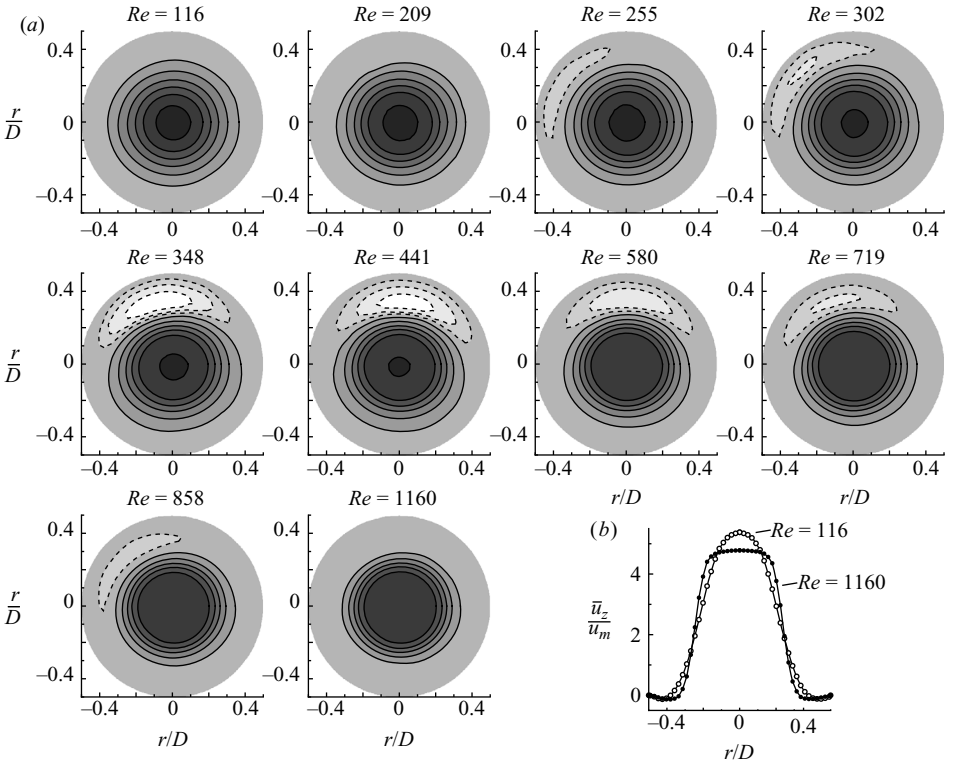

FIGURE 5. Normalized mean streamwise velocity in the section $z/D = 0.05$. (*a*) Variation of the velocity contours with Re. Continuous and dashed lines correspond to positive and negative values of velocity, respectively. (*b*) Radial velocity profiles for the two extreme Reynolds numbers.

Reynolds number is $Re = 116$, the smallest investigated, and the flow is observed to be steady. The streamlines show the presence of an axisymmetric recirculation region, which indicates that the flow separates in the diverging part of the constriction even for this low value of the Reynolds number. Velocity contours emphasize the presence of a laminar jet in the core of the flow resulting from the separation. The reattachment point is located approximately two diameters downstream of the exit plane of the constriction, and no velocity fluctuations occur in or downstream of the reattachment region.

Figure 5 presents flow characteristics in a cross-section located at $z/D = 0.05$ for various Reynolds numbers. Mean velocity properties were obtained by averaging over 800 instantaneous velocity vectors fields. The distribution of the mean streamwise velocity contours for $Re = 116$ indicates that the flow is axisymmetric downstream of the constriction. The velocity profile obtained in an azimuthal plane (figure 5*b*) shows details of the recirculation region surrounding the laminar jet in the core of the pipe flow. For $Re = 255$, the recirculation region concentrates on a distinct quarter of the cross-section (the dashed lines indicate reverse flow), and for larger values of the Reynolds number, the thickness of the separated region increases to reach a maximum at $Re = 348$. These results show that the flow symmetry breaks down at relatively low Reynolds numbers, which results in a deflection of the internal jet towards the pipe wall. When the Reynolds number is increased beyond a value of

https://doi.org/10.1017/S0022112008002188 Published online by Cambridge University Press

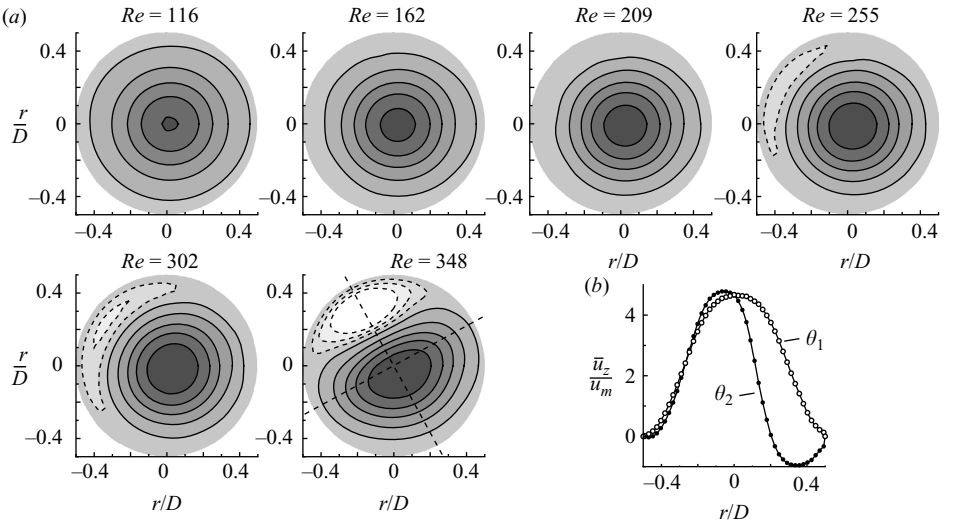

FIGURE 6. Normalized mean streamwise velocity in the section $z/D = 2.5$. (a) Variation of the velocity contours with Re. Continuous and dashed lines correspond to positive and negative values of velocity, respectively. (b) Radial velocity profiles for two azimuthal angles.

348, the spatial extent of the recirculation region gradually diminishes to return to symmetry for $Re = 1160$. This is clearly visible from velocity contours and the profile in figure 5(b). The present work focuse on a Reynolds number range of 116–1160 to study the asymmetry of the flow. It can also be observed that the location of the recirculation region, defined by the azimuthal angle where the velocity minimum is reached, depends on the Reynolds number and can shift position with flow rate changes. However, at this axial location, the flow remains steady.

Measurements have been repeated further downstream at $z/D = 2.5$ (figure 6a). For the smallest Reynolds number ($Re = 116$), a slight deflection of the jet was observed toward the upper right, even though the flow seemed symmetric at $z/D = 0.05$ (cf. figure 5) and in the meridional plane of figure 4. This leads to the conclusion that the flow asymmetry occurred at a Reynolds number lower than $Re = 116$. The deflection of the velocity maximum from the cross-section centre is less than $0.016D$, which remains very weak, so that measurements were not undertaken for lower Reynolds numbers. The degree of asymmetry increases with the Reynolds number to yield the characteristic streamwise velocity contour distribution observed for $Re = 348$. The dashed lines indicating reverse flow show that the recirculation region extens to more than half the radius. The streamwise velocity profiles plotted in figure 6(b) for the two selected azimuthal angles clearly show the asymmetry and the presence of the reverse flow. This indicates that two-dimensional data on a meridional plane must be interpreted with great care since the flow structure that is observed depends on θ. In particular, the profile obtained at $\theta = \theta_1$ contains no negative velocity values whereas the profile at $\theta = \theta_2$ shows the maximum extent of the recirculation region. The inflexion point in the θ_2 curve indicates that this flow might be unstable.

Figure 7(a) presents a global view of the flow at $Re = 348$ through contour plots of the streamwise velocity at several axial stations downstream of the constriction. The model has been rotated to place the recirculation region on the top of the three-dimensional plot to provide a better view of the flow. The thickness of the recirculation region is maximum at $z/D \approx 3$ and decreases in the downstream direction, but the

https://doi.org/10.1017/S0022112008002188 Published online by Cambridge University Press

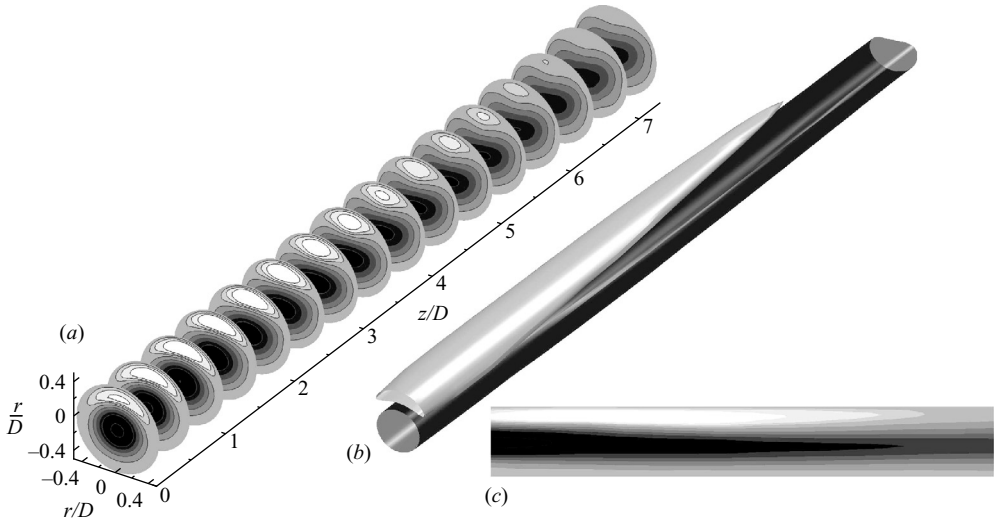

FIGURE 7. (*a*) Three-dimensional view of streamwise velocity contours for $Re = 348$. High and negative velocity levels appear in dark and light levels, respectively. (*b*) Isosurfaces of the same data, extracted for $\bar{u}_z/u_m = -0.4$ and 2. (*c*) Contours of velocity in the vertical meridional plane. A rotation around the pipe axis has been performed in order to best visualize the recirculation region.

flow has not recovered symmetry at the last measurement location available ($z/D = 7$). Isosurfaces of selected velocity levels (figure 7*b*) illustrate the shape of the confined jet and that of the recirculation zone visible on the top border of the plot.

These results indicate the presence of flow asymmetries for a range of Reynolds numbers even if the inlet velocity conditions are symmetric, which indicates the presence of a Coanda effect. The symmetry-breaking bifurcation is a phenomenon extensively reported in two-dimensional channels with symmetric sudden expansion (Fearn, Mullin & Cliffe 1990). On the contrary, to the authors' knowledge, it has never been measured before in axisymmetric geometries, even though this effect was captured numerically in the unsteady simulations of Sherwin & Blackburn (2005). However, comparison of the velocity contours obtained in the θ_2-meridional plane of symmetry (figure 7*c*) with results available in the literature shows that the deflection of the jet centreline is weaker in the axisymmetric configuration than in planar channel geometries. The weaker strength of the asymmetry implies that the phenomenon occurs on a restricted range of Reynolds numbers making it more difficult to detect in such geometries.

In the planar case, the fact that the flow attached on the upper or lower wall is due to small imperfections in the experimental arrangement, inherently present in any experimental setup. For higher values of *Re* the flow first becomes three-dimensional before becoming unsteady, the time dependence being a consequence of three-dimensional effects. In the present case, flow asymmetries are three-dimensional in nature since the geometry is axisymmetric. The backflow concentrates on a particular region of the pipe so that the general shape of the recirculation region is no longer a continuous ring. Varghese *et al.* (2007) used a geometry identical to ours but introduced a geometrical perturbation (a small eccentricity of the stenosis axis) which causes the jet to be deflected in the direction of the eccentricity. In the present experiment, we have observed that the direction of the flow asymmetry is influenced

https://doi.org/10.1017/S0022112008002188 Published online by Cambridge University Press

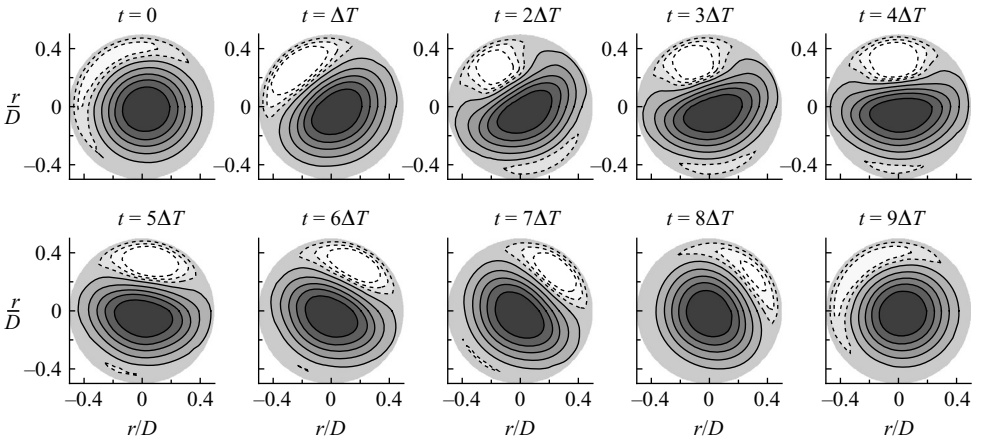

FIGURE 8. Evolution with time of instantaneous streamwise velocity contours obtained at $z/D = 2.5$ for $Re = 440$ and $\Delta T = 21D/u_m$. Continuous and dashed lines correspond to positive and negative values of velocity, respectively.

by the Reynolds number, i.e. it depends on the way the flow is established in the pipe. In the absence of asymmetry in the stenosis geometry, the deflection can occur in different directions in a preferred range of azimuthal angles rather than in a single direction. For example, the results presented in figure 5 were obtained during a single continuous run. The progression of the angular orientation of the symmetry breaking with the Reynolds number is random but limited in a given angular range imposed by small geometric imperfections.

Further increases of the Reynolds number indicate that, as expected due to the presence of an inflexion point in velocity profiles (see figure 6*b*), the flow becomes unsteady. $Re_c \approx 400$ appears to be the critical value below which the flow is steady; for $Re > Re_c$ instabilities kick in and intermittent signals are measured. This is the subject of the section below.

4. Onset of instabilities

Figure 8 shows the time evolution of instantaneous contours of streamwise velocity at $z/D = 2.5$ for $Re = 440$. The flow is no longer steady but exhibits low-frequency fluctuations. The thickness of the recirculation region increases between $t = 0$ and $t = 2\Delta T$. ΔT represents a time scale that is chosen independently for each plot of the paper to provide a better insight of the flow evolution with time. The occurrence of negative velocity levels at $t = 2\Delta T$ on the opposite side of the pipe indicates the presence of a second recirculation region. From $t = 2\Delta T$ up to $t = 6\Delta T$ the flow patterns remain approximately similar but undergo a solid-body clockwise rotation around the pipe axis. For $t \geqslant 7\Delta T$, the lower recirculation region disappears while the thickness of the upper recirculation region decreases. Finally, at $t = 9\Delta T$, the flow pattern suddenly switches back to its initial azimuthal location. The flow pattern is similar to the initial state observed at $t = 0$ and the phenomenon repeats itself.

These results highlight the presence of a cyclic process in the flow. The time scale of the phenomenon is very long, the oscillations having a period of $\sim 200D/u_m$ (a dimensional time of ~ 40 s). This oscillation begins with a growth of the recirculation zone followed by a swirling motion around the pipe axis. Asymmetric separations on

https://doi.org/10.1017/S0022112008002188 Published online by Cambridge University Press

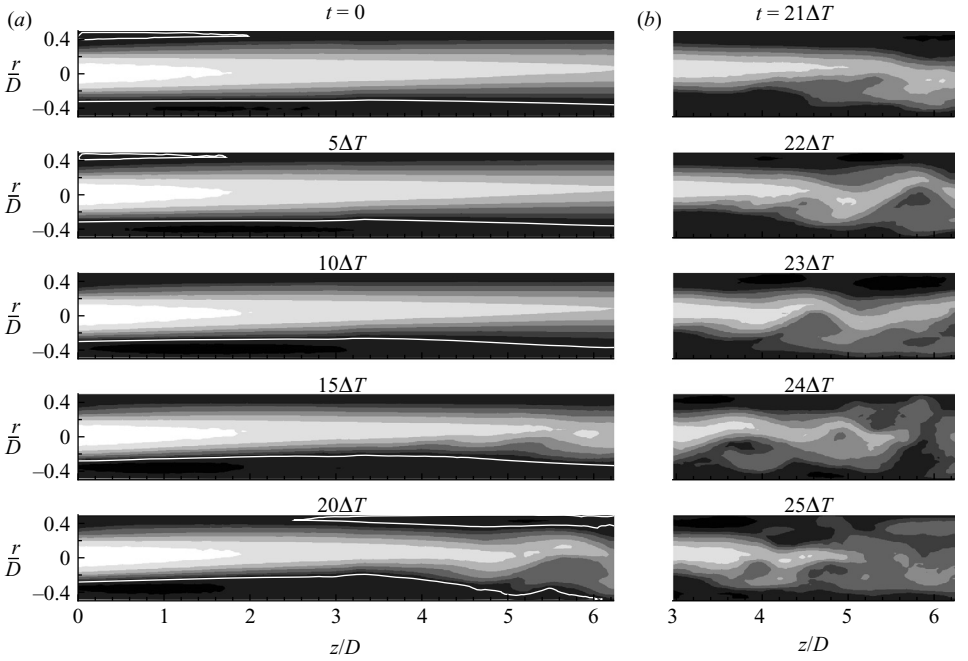

FIGURE 9. Evolution with time of instantaneous streamwise velocity contours for $Re = 440$ and $\Delta T = 0.94 D/u_m$. Measurements were obtained close to the symmetric meridional plane during (a) the growth of the recirculation region and (b) the swirling motion. Light to dark grey levels range from high to low velocity levels, and the white lines in (a) show isocontours corresponding to $u_z/u_m = 0$.

opposite parts of the cross-section are also observed. To provide qualitative insights into the large-scale flow unsteadiness, we performed two-dimensional time-resolved velocity measurements in meridional planes. We have chosen the symmetry plane going through the recirculation zone observed at $t = 0$ in figure 8 to plot in figure 9(a) contours of instantaneous streamwise velocity (note that the time scales ΔT between the two figures are different). Data are formed by two different sets of velocity vector fields placed side by side and the recirculation region appears in the bottom of the pipe. The time evolution of the flow structure clearly indicates the growth of the recirculation region for $t \leqslant 20\Delta T$. The white lines correspond to $u_z/u_m = 0$ and are plotted to highlight the approximate spatial extent of the separated zones. The presence of a second weaker recirculation on the top of the pipe is visible at $t = 0$ and $t = 5\Delta T$. As time increases, the main recirculation region grows at the expense of the weaker one which disappears at $t = 10\Delta T$. The curvature of velocity contour lines becomes increasingly pronounced, indicating that the flow approaches an unstable state. The onset of flow disturbances is observed at $t = 15\Delta T$ and their amplitudes grow with time. In addition, a new recirculation region appears at the downstream end ($z/D \geqslant 3$) near the upper wall at $t = 20\Delta T$, as was observed in figure 8. More details of the time evolution of the flow perturbations are shown in figure 9(b) for smaller time increments. The unstable character of the flow is confirmed by the growth of the instability. Waves are seen until $t = 24\Delta T$, together with high-frequency spatial fluctuations of the velocity field. At $t = 25\Delta T$, the flow structure is highly perturbed which could possibly indicate transition to turbulence.

https://doi.org/10.1017/S0022112008002188 Published online by Cambridge University Press

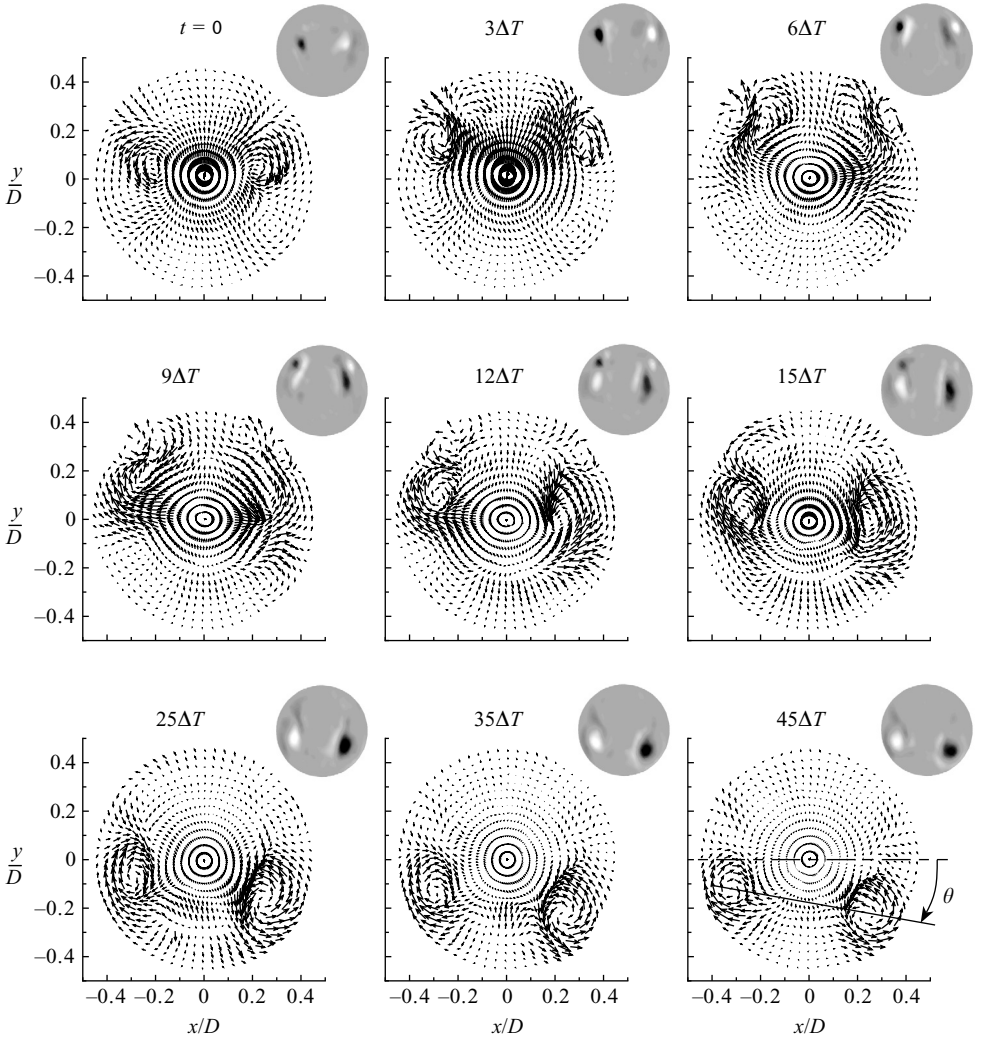

FIGURE 10. Time-varying vector fields of the in-plane wavelet velocity components at $z/D = 5.5$ for $Re = 440$ ($\Delta T = 0.038 D/u_m$), and associated streamwise vorticity contours (black and white levels corresponds to positive and negative vorticity).

The combined results of figures 8 and 9 show that instabilities occur before the onset of the swirling motion of the flow.

The growth of the recirculation region with time reveals that the mean flow characteristics depend on time, i.e. the flow is non-stationary. Wavelet transforms are used to separate the time-varying mean-flow variations (large-scale) from the small-scale fluctuations. Stereoscopic measurements were done at a streamwise location exhibiting high-amplitude flow perturbations. Figure 10 presents projections of wavelet fluctuating-velocity vector fields on the cross-section plane at $z/D = 5.5$. The time origin is chosen close to the onset of the instability. Initially, two counter-rotating vortices move toward the top of the pipe. For a better interpretation of the results the data at $t = 0$ were rotated around the pipe axis to align the vortices on

https://doi.org/10.1017/S0022112008002188 Published online by Cambridge University Press

the x-axis. All data at subsequent times have been treated in the same way. For $t \leqslant 3\Delta T$ the distance between the vortices increases, which highlight that under their mutual induction the vortices move away from each other. In contrast, when the pair of vortices approaches the wall ($3\Delta T \leqslant t \leqslant 6\Delta T$), the distance between them tends to decrease by the rolling of each vortex on the wall. The interaction of these two opposite movements progressively results in rollup of vorticity layers followed by the formation of new compact streamwise vortices. The new pair of vortices appears at $t = 6\Delta T$, develops for latter times and is particularly visible for $t \geqslant 15\Delta T$. The motion of the primary vortex pair tends to initially pull the two newly formed secondary vortices towards each other and in the direction of the upper wall. Since this movement occurs against their own mutual induction, this results in a lift up of the secondary vortex pair from the upper wall and the two vortices move away from each other in the direction of the lower wall.

Streamwise or quasi-streamwise secondary vortex generation close to primary streamwise vortices is a frequently observed phenomenon in wall-bounded flows (a description of the process can be found in the direct numerical simulation of wall turbulence of Zhou *et al.* 1999, together with a review of previous studies on the subject). In the present case, the onset of instabilities is accompanied by the formation of coherent streamwise vortices. They develop in the flow and interact with the wall which creates new streamwise vorticity concentrations. In figure 10, the strength of the primary vortex on the left is higher than that of the right vortex. The interaction between the vortices and the wall induces a clockwise rotation of the bulk flow: the line plotted at $t = 45\Delta T$ shows that the axis passing by the centres of the newly formed vortices is tilted at an angle θ to the horizontal axis of the initial alignment of the primary vortices. This results in a small rotation of the flow pattern around the pipe axis. After the formation of the secondary vortex pair, they convect and finally meet the opposite wall, which can lead to the formation of tertiary vortices by the same scenario depending on the strength of the vortices. Hence, the cumulative effects of the successive generation of new streamwise vortices induces the slow swirling flow motion. The swirling movement occurs along with the formation of coherent vortex structures. In fact, for large times following the development of the instability, the frequency of vortex generation increases, multiple streamwise vortex pairs appear simultaneously at different time intervals and directions together with a loss of coherence. Thus, this random process leads on average to the disappearance of global swirling motion. Iribarne *et al.* (1972) observed, for a sudden expansion pipe flow, that the flow acquired a substantial circumferential component in the reattachment zone. This coincides with the present low swirling movement. In their experiments on a sinusoidal-shaped stenosis, Ahmed & Giddens used a laser Doppler anemometer to obtain velocity time signals. In their experiment for $Re = 1000$ with 50 % area reduction (Ahmed & Giddens 1983*a*) they reported disturbances at a discrete frequency corresponding to a Strouhal number $\sim$0.16 (based upon conditions at the throat), and for $Re = 2000$ (Ahmed & Giddens 1983 *b*) they observed at $z/D = 1.5$ large irregular oscillations of the axial velocity with a peak-to-peak amplitude as high as $\sim u_m/2$ at a Strouhal number as low as $\sim$0.12. However, the Strouhal numbers associated with vortex shedding have values above 0.4 and then are high compared to all the precedent values. These observations indicate that velocity oscillations are incompatible with the occurrence of vortex shedding, as inferred by the authors. It is possible that the signal was the result of a solid-body rotation of an asymmetric mean flow. Similarities observed with time traces such as those extracted from the data of figure 8 support this explanation.

https://doi.org/10.1017/S0022112008002188 Published online by Cambridge University Press

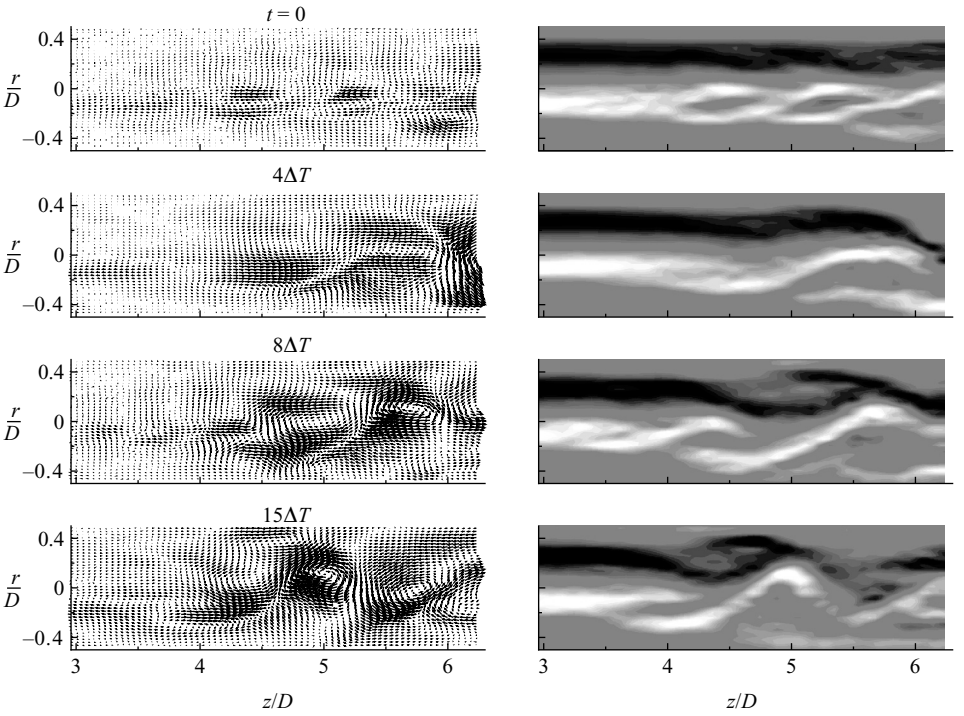

FIGURE 11. Selected velocity vector fields and associated spanwise vorticity in the meridional plane for $Re = 440$ and $\Delta T = 0.47 D/u_m$.

The evolution of the instability in the downstream portion of the pipe can be followed in the meridional planes plotted in figure 11. A selection of instantaneous fluctuating-velocity vector fields is presented with their respective spanwise vorticity fields. The $t = 0$ plot shows instability waves associated with shear-layer oscillations induced by the deflected jet. At longer times the flow unsteadiness increases and the formation of local rotation patterns is observed. The presence of eddies is particularly visible at $t = 8$ and $15\Delta T$ and their centres coincide with the locations of high-vorticity concentration (in white). In addition, each eddy seems to be followed upstream by a streak line forming a leg to the spanwise structure. The next section describes the nature of these vortices.

5. Vortex identification

5.1. *Methodology*

To highlight the spatial structure of the unsteady flow, we apply an approximate three-dimensional method of vortex identification. Measurements obtained in the stereoscopic arrangement provide the two in-plane and the out-of-plane velocity components in cross-section coordinates. To estimate data in the streamwise direction, we use the Taylor hypothesis. The time-history of the flow as seen from a fixed reference frame can be viewed as the advection of a frozen spatial structure travelling with the convection velocity u_c, so that the time is replaced by a spatial coordinate, i.e. $\boldsymbol{u}(z, t) = \boldsymbol{u}(z - u_c t, 0)$.

Spatial derivatives relative to the axial coordinate are obtained with the Taylor hypothesis according to $\partial_z = -u_c^{-1}\partial_t$. An estimate of the convection velocity u_c was computed from the two-point correlation function, yielding $u_c/u_m \simeq 2$. Considering

https://doi.org/10.1017/S0022112008002188 Published online by Cambridge University Press

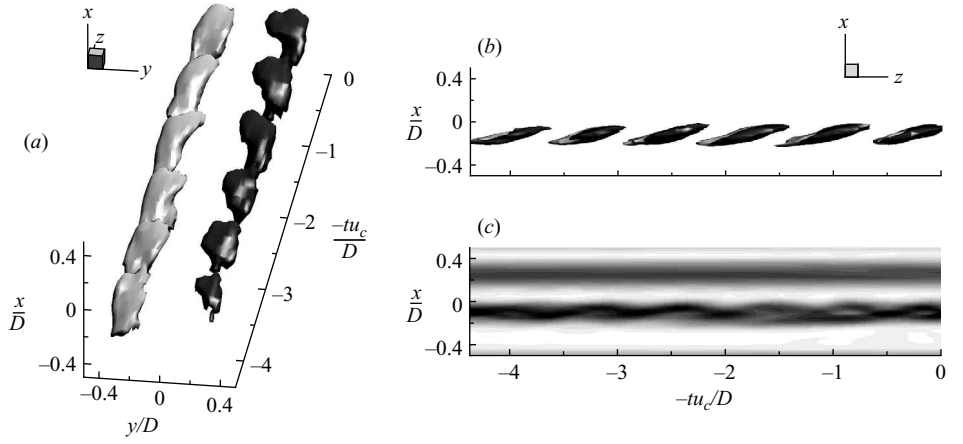

FIGURE 12. Vortex pattern identified at $z/D = 4$ for $Re = 460$: (*a*) three-dimensional perspective view of isosurfaces of $\omega_z = \pm 40\,\%$ of maximum (black positive, white negative); (*b*) side view; (*c*) contours of $|\boldsymbol{\omega}|$ in the plane of symmetry $y/D = 0$.

the sectional-averaged velocity u_{max} in the throat of the constriction, the ratio simply becomes $u_c/u_{max} \simeq 0.5$. This value was found to be insensitive to the Reynolds number.

The λ_{ci}-based criterion, referred to the local swirling strength by Zhou *et al.* (1999), is used as the vortex extraction technique. The thresholding of λ_{ci} throughout the paper is chosen to best visualize vortical structures, but the vortical pattern is not affected by the choice of the λ_{ci} value, which is non-dimensionalized with u_c and D.

5.2. *Results*

Figures 12–14 present a selection of vortex structures identified during different development stages of the instability. In figure 12, results correspond approximately to the onset of velocity fluctuations at $z/D = 4$ for $Re = 460$. Figure 12(*a*) shows a three-dimensional perspective view of vortices visualized through isosurfaces of the streamwise vorticity ω_z. The streamwise direction is scaled by $-tu_c/D$ and the initial time is arbitrary, recalling that by using the Taylor hypothesis the flow structure is frozen. The vortex topology is composed of elongated vorticity filaments aligned with the streamwise direction. Each negative vorticity pattern can be associated with a positive vorticity pattern to form a vortex pair. The overall structure can be described by the development of contra-rotating quasi-streamwise vortices of weak intensity. Due to the quasi-symmetry of the vortex pairs, a solid-body rotation of the data around the pipe axis was applied to place the symmetry plane in the vertical direction. This rotation will be applied to all similar plots in the remainder of the paper. This geometric transform defines the x- and y-axes of the cross-sectional planes to present side views compatible with figure 12(*b*). In figure 12(*b*) the vortex pairs are characterized by a constant inclination angle with respect to the horizontal axis. In each vortex pair, since the spanwise distance (i.e. on the y-axis) is slightly shorter in the downstream region compared to the upstream region, the induced velocity field in the downstream region is stronger and induces a lift motion near the vortex downstream ends. The last plot (figure 12*c*) presents the same flow as in figure 12(*b*) but in the form of contours of the vorticity magnitude $|\boldsymbol{\omega}|$ in the meridional plane $y/D = 0$. This plane does not intersect vortices but highlights signatures of vortical structures in the symmetry plane. The vorticity magnitude shown is essentially composed of azimuthal vorticity and remains weak in these early stages of the instability development.

https://doi.org/10.1017/S0022112008002188 Published online by Cambridge University Press

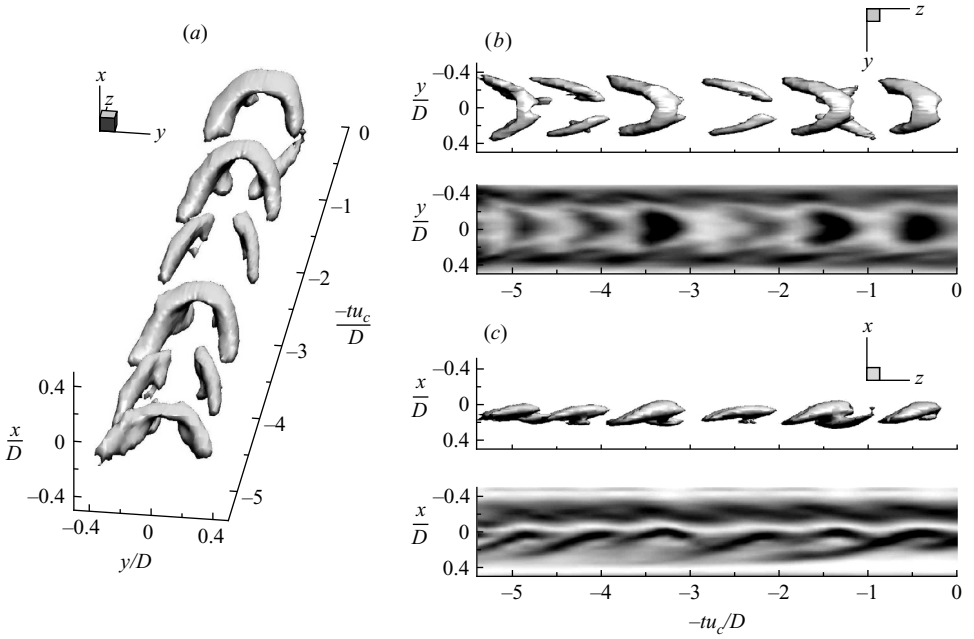

FIGURE 13. Vortex pattern identified at $z/D = 5$ for $Re = 460$: (*a*) three-dimensional perspective view of isosurfaces of $\lambda_{ci} = 2$ (non-dimensionalized with u_c and D); (*b*) top view with contours of $|\boldsymbol{\omega}|$ in the plane $x/D = 0$; (*c*) side view with contours of $|\boldsymbol{\omega}|$ in the symmetry plane $y/D = 0$.

An important point in the present visualizations is that the validity of the Taylor hypothesis can be qualitatively verified by comparing the extrapolated three-dimensional view with measurements in a plane. The vorticity map of figure 12(*c*) presents some similarities with the spanwise vorticity plot of figure 11 ($t = 0$), which indicates that the shear-layer development is accompanied by the formation of quasi-streamwise vortex pairs in the flow. Thus velocity data extracted from a meridional plane can be qualitatively interpreted if the corresponding vortex signature is retrieved via the Taylor hypothesis.

The second example, illustrated in figure 13, identifies vortical structures at a later stage of the instability amplification process. The evolution of the vortex pair is shown in figure 13(*a*) with isosurfaces of $\lambda_{ci} = 2$. It indicates that the spanwise distance between the quasi-streamwise vortices is shorter at the downstream end than at the upstream end. The high mutual induction combined with the short spanwise separation leads to the appearance of connections between some of the vortex pairs. These connecting regions are essentially composed of spanwise vorticity and give to vortex pairs a characteristic Λ-shape, clearly seen in the top view of figure 13(*b*). The contours of $|\boldsymbol{\omega}|$ in the plane $x/D = 0$ in figure 13(*b*) show a characteristic vortex signature and are reminiscent of vortex bursts observed in transitional boundary layers. Additionally, comparisons of the vorticity contours in the bottom view of figure 13(*c*) with those of figure 11 for $t = 4\Delta T$ and $t = 8\Delta T$ show that the wavelength of the flow perturbation is quite similar for the two figures.

More developed structures are shown in figure 14 for data obtained at $z/D = 5.5$ and $Re = 460$. The perspective view in figure 14(*a*) shows the presence of several vortices of various forms and sizes identified with the terminology of Robinson (1991). Most

https://doi.org/10.1017/S0022112008002188 Published online by Cambridge University Press

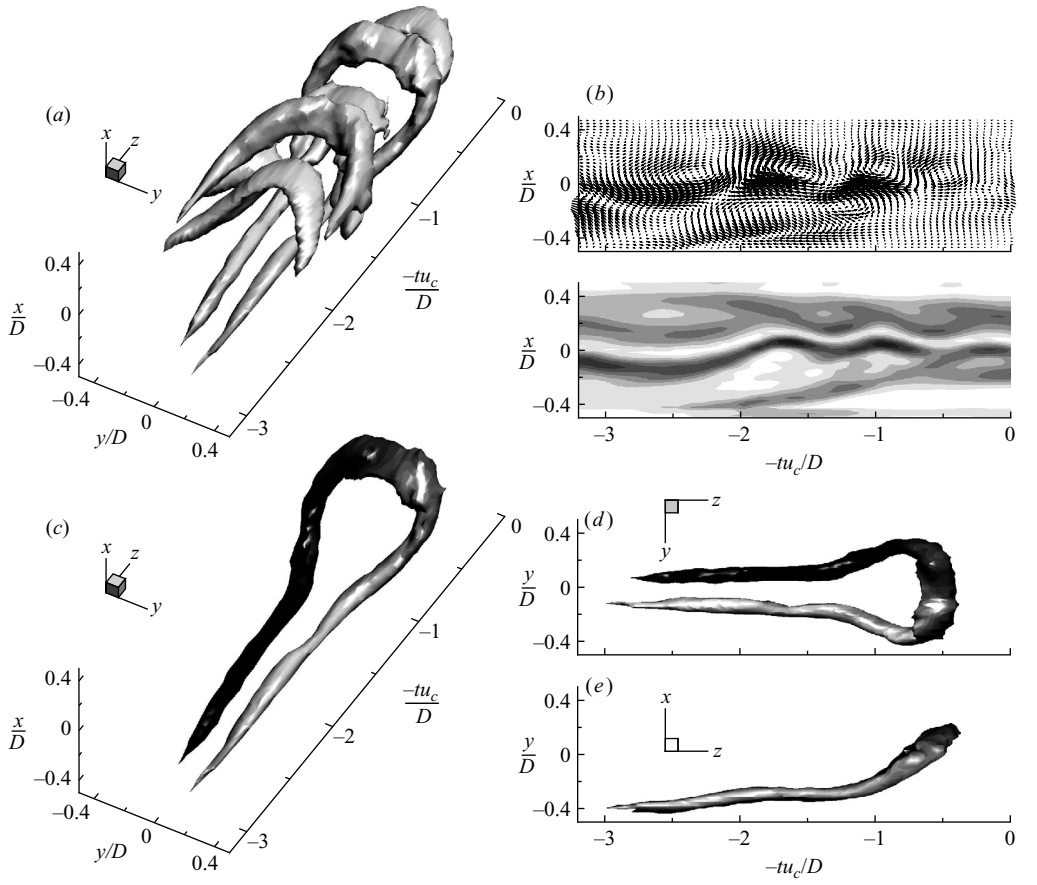

FIGURE 14. Vortex structures extracted at $z/D = 5.5$ for $Re = 460$: (a) perspective view of isosurfaces of $\lambda_{ci} = 2.5$; (b) wavelet fluctuating-velocity vectors and contours of $|\boldsymbol{\omega}|$ in the plane $y/D = 0$. The biggest vortical structure in (a) has been extracted for a better visualization and is shaded with contours of ω_z (black positive, white negative): (c) perspective view; (d) top view; (e) side view.

vortices present a general arch-shape structure with concentrated spanwise vorticity forming a head, followed by a neck of varying length, which can be assimilated to horseshoe vortices. One of these coherent structures is shown in figures 14(c–e) for a better visualization. The arch and neck of the vortex form a Ω-shape head connected to a pair of counter-rotating quasi-streamwise vortices forming long legs trailing behind. These structural features are typical of a hairpin-like vortex commonly encountered in laminar and turbulent boundary layer flows. However, contours of ω_z show that the rotational motion of the vortex identified in figure 14(c) is opposite to that of the classical models of the literature. Several factors can explain this feature. First, as described in figure 10, the unsteady flow can generate vortex pairs with opposite rotations. Second, the internal jet is subject to swirling or flapping motions which can lead to the rotation of a structure around the pipe axis. Third, when the flow exhibits velocity fluctuations above the critical Reynolds number, figure 9 indicates the presence of a recirculation region on each side of the pipe. Therefore, even if the flow asymmetry induces a shear-layer development between the main flow and the recirculation region on the lower wall, the presence of an outer wall induces a

https://doi.org/10.1017/S0022112008002188 Published online by Cambridge University Press

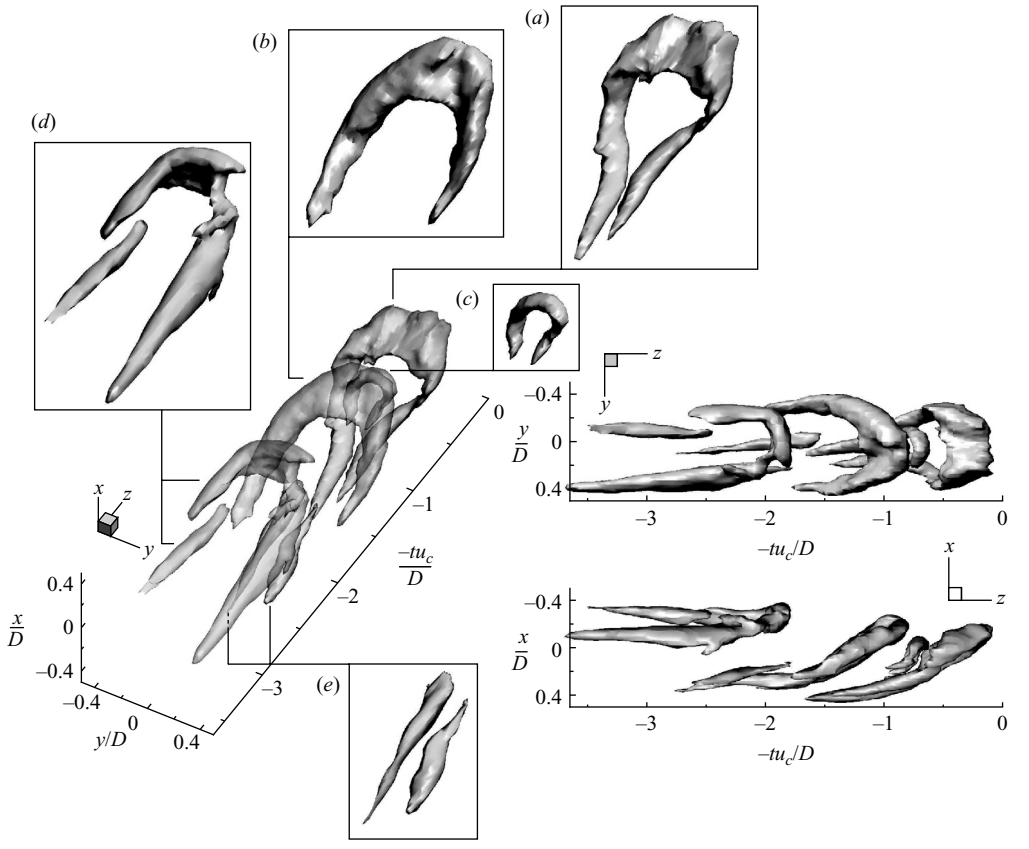

FIGURE 15. Vortex structures extracted at $z/D = 5.5$ for $Re = 460$. The central plot is a perspective view and on the right top and side views are presented. Frames (*a–e*) are used to visualize individually each of the vortices extracted from the central vortex pattern.

shear flow also between the main flow and the upper wall. All these factors highlight the complexity of the flow. Hence, the vortex identified here is considered to belong to the hairpin-like structure family.

The fluctuating-velocity vector and vorticity fields in the symmetry plane $y/D = 0$ shown in figure 14(*b*) exhibit strong similarities with features of figure 11 at $t = 15\Delta T$, and are characteristic of the signature of hairpin vortices. Following Robinson (1991), the head of a hairpin vortex induces a local flow rotation and below the structure a region of low momentum is induced by the cumulative effects of the head and neck. A close examination of figure 14(*b*) clearly shows these characteristics for two arch vortices for which the velocity vectors indicate local rotation (see also figure 11). This ejection process corresponds to the occurrence of a Q2 event, a region of strong second-quadrant vectors ($u_z' < 0$, $u_r' > 0$) in the midplane of the hairpin vortex. Finally, the legs represent regions of concentrated streamwise vorticity and contribute to induce low momentum upward and low-speed streaks. When the backflow encounters the mean flow, an inclined shear layer is observed to form upstream. Again, by examining figures 11 and 14(*b*), the local circular rotation regions are clearly followed by stagnation lines characteristic of the presence of local shear layers.

To properly locate hairpin vortices based on the identification technique, figure 15 presents a last example of flow pattern ($z/D = 5.5$, $Re = 460$). The perspective view

https://doi.org/10.1017/S0022112008002188 Published online by Cambridge University Press

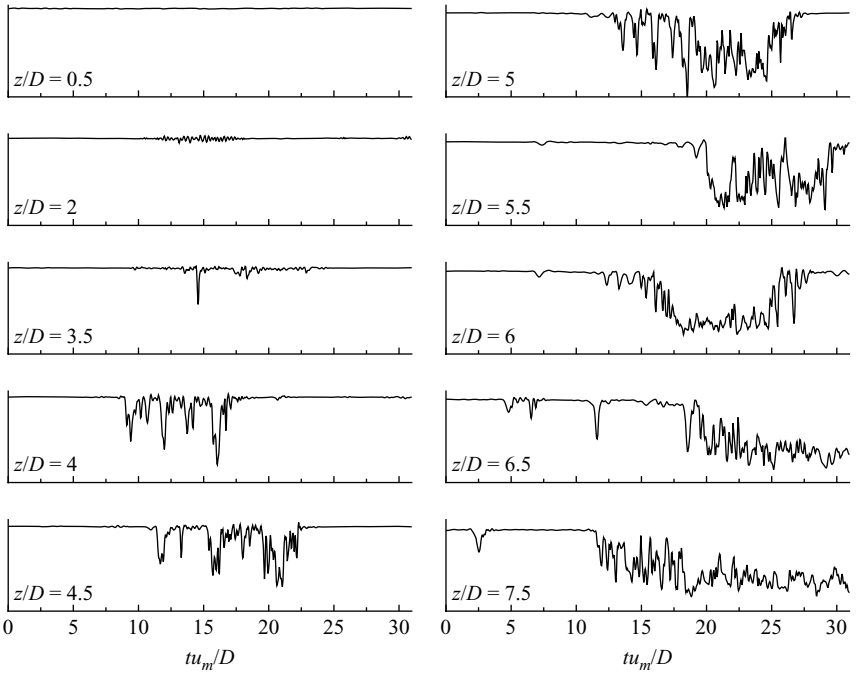

FIGURE 16. Evolution with z/D of $u_z(t)$ signals obtained at $r/D = 0$ for $Re = 720$. Note that the time traces have not been acquired simultaneously.

shows several vortical structures rendered as translucent isosurfaces of λ_{ci} whose value has been varied to achieve the best visualization for each vortex. The exploded view highlights the rich flow features. The structure in figure 15(a) is a Ω-shaped vortex and in figure 15(b) the pattern is close to a horseshoe vortex. Between these two structures, in figure 15(c) is a small Ω-shaped vortex. Adrian, Meinhart & Tomkins (2000) refer to all of these vortices by the unique terminology of hairpin-like structure, which can represent deformed versions of a common basic structure at different stages of evolution. Figure 15(a–c) illustrates the variety of sizes, whereas the cane-vortex of figure 15(d) shows a different shape induced by the degree of asymmetry. Finally, the presence of a pair of counter-rotating quasi-streamwise vortices is shown in figure 15(e). The next section will focus our attention on the question of investigating the various flow regimes.

6. Transition to turbulence

6.1. *Non-stationary flow*

Figure 16 presents instantaneous streamwise velocity time signals for different longitudinal positions on the pipe axis for $Re = 720$. In the vicinity of the stenosis outflow section ($z/D = 0.5$), the velocity remains constant throughout the time interval investigated (0–30). Small velocity fluctuations around the mean appear at $z/D = 2$ and are localized in time, as observed at $z/D = 3.5$. Downstream of this position, velocity fluctuations are more pronounced, with large negative velocity peaks. However, the perturbations remain localized in time. For $z/D \geqslant 5$, flow perturbations are especially pronounced and seem to indicate that the mean-flow properties have changed. For example, at $z/D = 6$, the velocity signal fluctuates for $18 \leqslant tu_m/D \leqslant 25$

https://doi.org/10.1017/S0022112008002188 Published online by Cambridge University Press

around a mean that is less than the constant value found at $t = 0$. This results in a characteristic signal form composed of two velocity scales, a high mean-velocity level with no perturbations and a low mean-velocity level presenting high-intensity fluctuations. The two last signals ($z/D = 6.5$ and 7.5) show that the time interval for which velocity fluctuations develop increases significantly compared to upstream locations. Thus the flow fluctuations and the mean-flow variations increase with the downstream position.

Figure 17(a) shows contour plots of the mean streamwise velocity component $\tilde{u}_z$ and the corresponding vector plots of the fluctuating velocity in a meridional plane ($Re = 720$). The snapshots were selected to highlight the decreasing extent of the internal jet in the time interval considered. This explains the change in the mean-flow properties in this region. Additionally, the axial movement of the jet is associated with spatial velocity fluctuations in the vector plots. These fluctuations are analysed in figure 17(b) by tracking the continuous wavelet transforms of the radial velocity registered at regularly spaced locations along the pipe axis (note that figures 17a and 17b are for the same velocity data sets). The semilog plot at $z/D = 3$ shows that the wavelet coefficients are close to zero except for a small interval around $tu_m/D = 20$, indicating the presence of low-amplitude velocity fluctuations that are localized in time. The occurrence of velocity perturbations at this location suggests that the flow fluctuates for all positions downstream. This is verified by the velocity vector plot of figure 17(a) at the corresponding time and by all subsequent wavelet transforms on figure 17(b). At $z/D = 3.4$, $|W_{u_r}(t, f)|$ contains a wider spectrum of frequencies and shows the first indication of high-frequency oscillations in the flow. As one moves to downstream locations, the patch of high-frequency fluctuations covers a increasingly wider time interval to reach the state observed at $z/D = 6.2$. Almost all the time–frequency plane is composed of high-frequency fluctuations, which is typical of turbulent flows. This plot also exhibits a localized region around $tu_m/D = 5$ characterized by low-frequency perturbations. This coincides with the plot of figure 17(a) at the same instant for which there are almost no spatial velocity fluctuations.

Continuous wavelet transforms indicate that the turbulent breakdown arises at different axial positions and times. An example of localization in space and time of the turbulent front is shown in figure 18, which presents combined results of two- and three-dimensional measurements of the streamwise velocity. Stereoscopic measurements acquired at two axial locations are shown for two instants. These instants were selected to illustrate the flow regimes where low- and high-amplitude velocity fluctuations are observed. Three-dimensional perspective views in a meridional plane provide a better idea of the spatial organization of the flow. Figure 18(a) shows the instantaneous mean flow properties through the spatial distribution of $\tilde{u}_z/u_m$, whereas figure 18(b) shows the corresponding instantaneous fluctuating velocities u'_z/u_m. For the first instant (plots on the left), the jet is clearly visible in the cross-section plot and remains laminar throughout the region since only weak velocity fluctuations are detected. A slight asymmetry is present but is not as pronounced as in the case of steady flow. However, the recirculation region, appearing on both sides of the wall, extends out of the measurement zone. The instantaneous mean properties drastically change when the same region is investigated at a time where the flow shows oscillations (plots on the right). Cross-section plots show a strong asymmetry at $z/D = 3$. Hence a recirculation region is shifted to the right of the pipe while the jet is deflected to the left. The central core of the jet decays quickly downstream along the axis of the pipe. At $z/D = 6$, the velocity profile is flat. Flattening is accompanied

https://doi.org/10.1017/S0022112008002188 Published online by Cambridge University Press

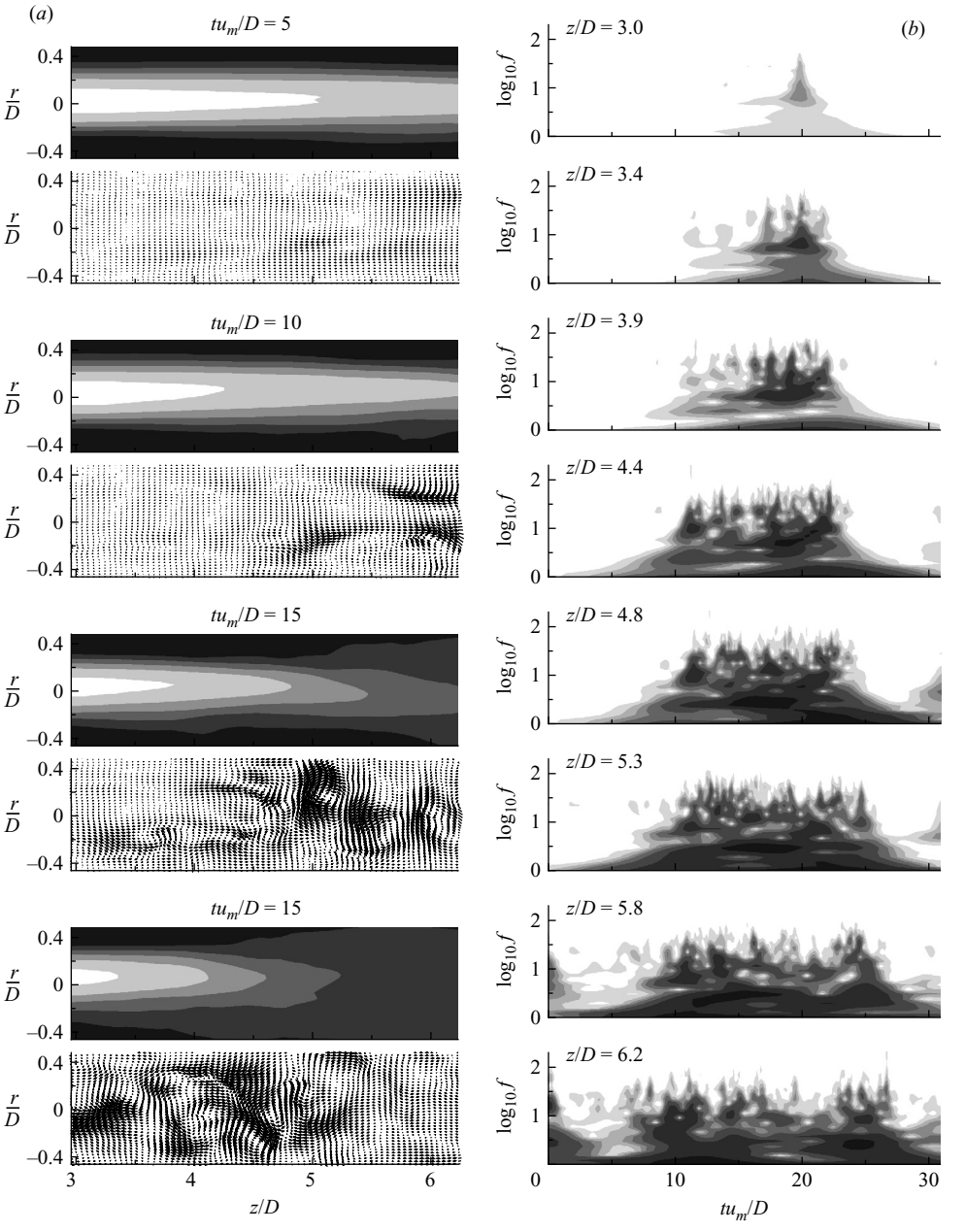

FIGURE 17. (*a*) Contours of $\tilde{u}_z$ and associated fluctuating velocity vector fields in a meridional plane obtained at different times for $Re = 720$ (light to dark grey levels range from high- to low-velocity levels). (*b*) Continuous wavelet transforms $|W(t, f)|$ of $u_r(t)$ extracted from (*a*) for different axial locations at $r/D = 0$.

by an increase in the amplitude of the spatial perturbations of the profiles of u'_z/u_m in the streamwise direction. This indicates that the flow undergoes a local transition to turbulence. However, as observed previously and indicated in the time trace of figure 18(*a*) at $z/D = 6$, this state is temporary since the flow returns to a laminar flow regime further downstream and at later times.

https://doi.org/10.1017/S0022112008002188 Published online by Cambridge University Press

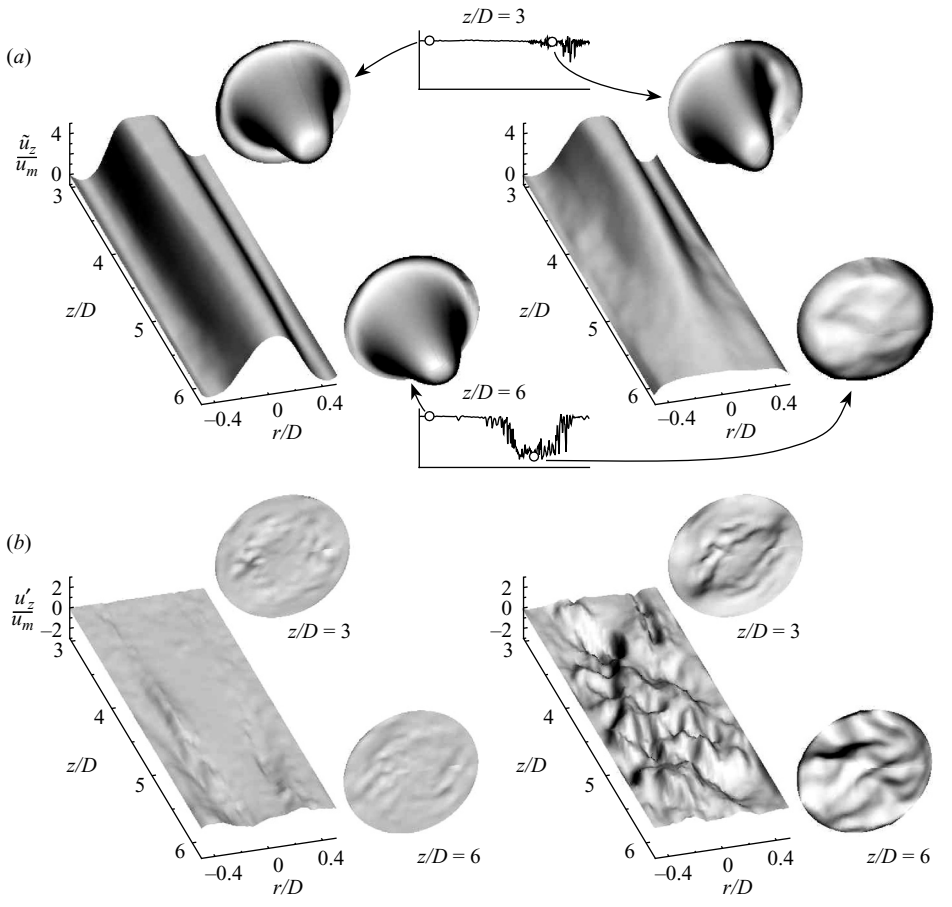

FIGURE 18. (*a*) Perspective views of $\tilde{u}_z/u_m$ obtained from cross-sectional measurements at $z/D=3$ and $z/D=6$ for two chosen instants appearing as dots in velocity–time traces and corresponding to the laminar and turbulent flow regimes ($Re=720$). Results of two-dimensional measurements were selected in order to approximately match the cross-sectional results. (*b*) Same as (*a*) but with the instantaneous velocity profiles of u_z'/u_m.

Previously we showed that the development of unsteady perturbations is associated with an apparently gradual increase of the volume of the recirculation region (cf. figure 9). Figure 19 shows that this phenomenon also occurs in an inverse manner. Contours of the mean streamwise velocity $\tilde{u}_z$ are mapped for $Re=630$ to follow the time evolution of the mean properties of the recirculation region. Each plot corresponds to an instant marked by a circle on the time signal of u_z ($z/D=3$, $r/D=-0.25$) in figure 19(*a*). At $t=t_0$, velocity fluctuations are associated with a relatively thick and short recirculation region. For larger values of time, the progressive disappearance of unsteadiness is accompanied by an increase of the length of the recirculation zone which extends outside of the plots, as observed for $t \geqslant t_0+4\Delta T$. However, the flow continuously evolves as indicated by the regular decrease of the velocity for $t_0+3\Delta T \leqslant t \leqslant t_0+7\Delta T$ (figure 19*a*). During this time interval the velocity becomes negative and contour plots show an increase of the thickness of the recirculation region. Following this, velocity fluctuations appear which coincide

https://doi.org/10.1017/S0022112008002188 Published online by Cambridge University Press

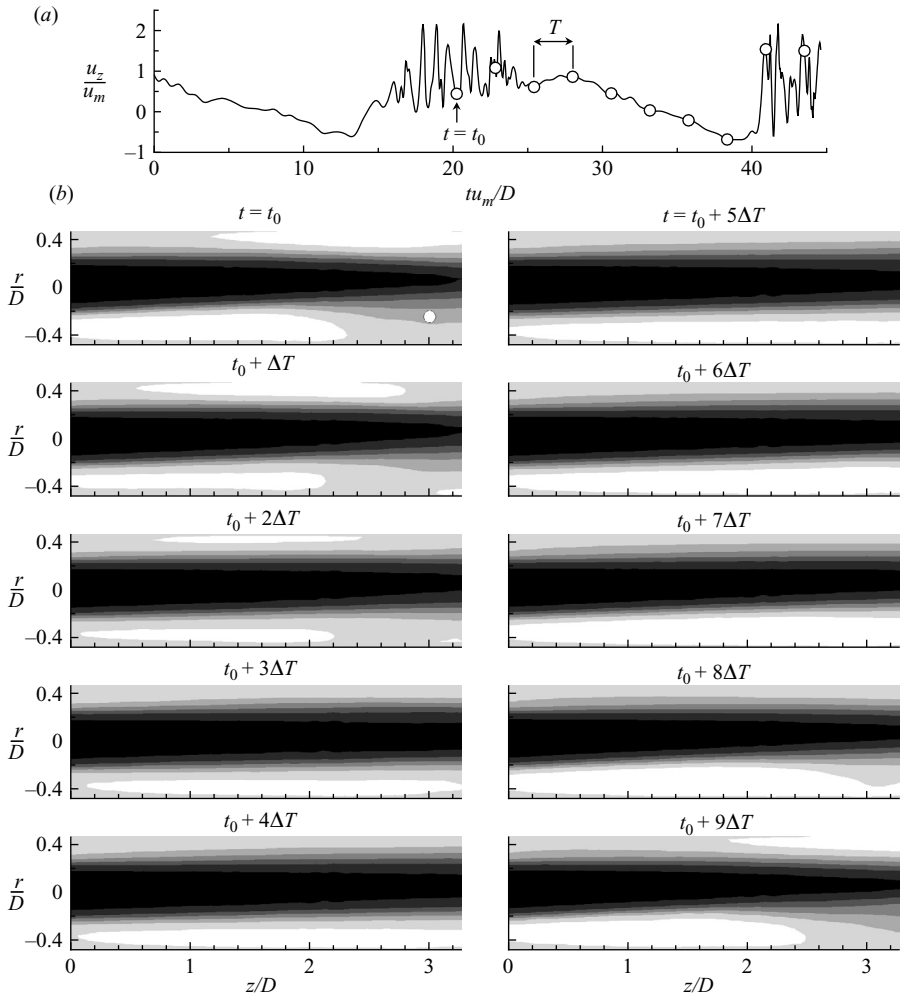

FIGURE 19. (*a*) Streamwise velocity time signal extracted at $z/D = 3$ and $r/D = -0.25$ for $Re = 630$. (*b*) Evolution of $\tilde{u}_z$ contours with time for instants marked with a white dot in (*a*) ($\Delta T = 2.6D/u_m$). The location where the time trace has been obtained is also shown with a dot in the map at $t = t_0$. Negative velocity regions appear in white.

with an abrupt decrease of the length of the recirculation region. The flow structure observed at $t = t_0 + 9\Delta T$ is similar to that at $t = t_0$.

The back and forth motion of the reattachment point can be explained as follows. For small Reynolds numbers, the jet attaches to the wall and establishes a non-axisymmetric recirculation region past the stenosis. The asymmetry increases with the Reynolds number and becomes severely pronounced. The deflection of the jet from its centreline induces strong inflexion points on velocity profiles. The thickness of the recirculation region increases at the expense of its length. With further increases of the Reynolds number, the curved streamlines are unable to remain attach and the flow becomes unsteady and forms vortical structures leading to turbulence. As the fluid in the separated region is continuously entrained into the main flow by the shear layer, the flow recovers its stability immediately past the constriction. The reattachment point moves downstream and the thickness of the recirculation region decreases.

https://doi.org/10.1017/S0022112008002188 Published online by Cambridge University Press

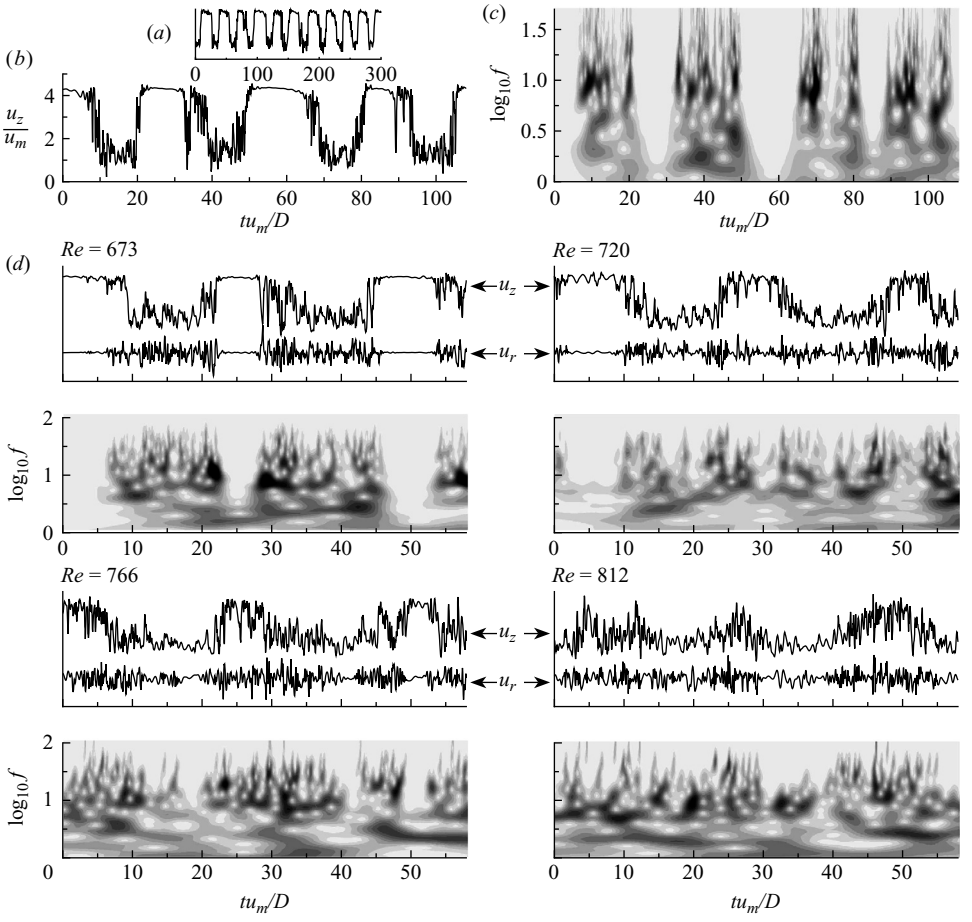

FIGURE 20. (*a*) Typical velocity signal form of $u_z(t)$ acquired at $z/D = 5$ and $r/D = 0$ for $Re = 630$ registered during a long acquisition time with a small sample frequency. (*b*) Detail of the same signal obtained for a higher sampling frequency for which the continuous wavelet transform is shown in (*c*). (*d*) Influence of the Reynolds number on the $u_z(t)$ (upper trace) and $u_r(t)$ (lower trace) velocity forms extracted at the same location as in (*a*) and associated contours of $|W_{u_r}(t, f)|$.

There again the Coanda effect deflects the internal asymmetric jet (its asymmetry is maintained by the resulting cross-flow pressure gradient in the steady region), and the process repeats itself indefinitely. Thus, at moderate Reynolds numbers, the cyclic discharge of mass from the recirculation region induces successive phases of steady, unsteady and turbulent flow, before returning to a steady regime. This explains the apparent periodic nature already seen in the results of figure 8. To provide an idea of the frequency of the phenomenon and its periodicity, figure 20(*a*) shows a typical time–velocity signal at $Re = 630$ measured on the pipe axis during a long period. The time trace clearly shows periodicity of the phenomenon. A close-up view of these oscillations is shown in figure 20(*b*) and indicates that the flow alternates between two velocity levels. The upper velocity level is closed to $4u_m$, the sectional average velocity in the throat of the stenosis. This corresponds to the centreline velocity of the internal jet indicating that the flow is laminar. The lower velocity level is associated with high-frequency flow fluctuations as observed in the continuous wavelet transform of

https://doi.org/10.1017/S0022112008002188 Published online by Cambridge University Press

figure 20(*c*). It is slightly greater than the average velocity u_m, indicating that, in this case, the streamwise velocity is uniform in the section and that the flatness of the velocity profiles is due to a breakdown to turbulence.

The process described here completes the scenario given by Sreenivasan & Strykowski (1983) who observed characteristic oscillations in a sudden expansion pipe flow for similar Reynolds numbers. They also noted that any perturbation inserted upstream of the expansion (even as seemingly small as a dye injection needle a few tenths of millimetre in diameter) destroyed the oscillations and stabilized the reattachment point and the transition to turbulence at a fixed location closer to the sudden expansion. Cassanova & Giddens (1978) studied the flow through a smooth occlusion formed by intersecting circular arcs, with an entry profile not fully developed. They reported, using a dye visualization technique, flow instability downstream of the recirculation region for $Re = 635$, which was attributed to a vortex breakdown. Although the dye was injected on one side of the shear layer and could potentially destroy large oscillations, they concluded vortex rings were present. Our experiments show that the flow behaviour is much more complicated due to large spatial and temporal intermittencies in local laminar and turbulent regions.

Additional results on the two components of the in-plane velocity vector extracted from two-dimensional measurements are shown in figure 20(*d*) for the same experimental conditions but for higher Reynolds numbers. At $Re = 673$, the flow oscillations identified previously are present on the trace of $u_z(t)$ and behave like turbulent puffs in $u_r(t)$ around a zero mean velocity. However, laminar stages occur less frequently and their duration is shorter compared with those at $Re = 630$. A transition is observed when the Reynolds number is increased to $Re = 720$ because the upper velocity level in $u_z(t)$ is characterized by fluctuations. The corresponding $u_r(t)$ signal also shows the flow perturbations over the complete time trace. The wavelet transform reveals that only the first part of the signal contains low-frequency components, whereas mostly only high frequencies are present for all the rest of the signal. Alternate phases of low and high frequencies are also observed at $Re = 766$ but oscillations have lost their regularity. The last example at $Re = 812$ shows that oscillations are difficult to detect and that the characteristic two-level velocity signals have almost disappeared.

To confirm this observed trend, time traces of streamwise velocity have been acquired at a downstream location $z/D = 7.5$ on the pipe axis. Figure 21 presents such traces for several Reynolds numbers. The first trace is for $Re = 441$, a value close to the critical Reynolds number beyond which unsteady effects appear. Oscillations are not regular at this downstream location. In fact, the signal presents a long laminar phase, a local transition to turbulence (where the mean velocity drops) and additional intermediate stages characterized by high-frequency velocity fluctuations. Increasing the Reynolds number increases the frequency of occurrence of turbulent events; however, no general trend can be discerned due to the high intermittency of time series. For $626 \leqslant Re \leqslant 766$, the results show that the relatively long laminar flow regimes are progressively replaced by fluctuations of short duration rapidly alternating from the high to the lower-velocity levels. As the Reynolds number reaches 812, the signal includes only a few transient parts and for $Re \geqslant 928$, the flow exhibits no intermittency and the velocity fluctuates randomly around a mean close to the sectionally averaged velocity.

Comparisons of time traces between the axial locations of figures 20 and 21 indicate that the regularity and repeatability of oscillations depend on the location of the probe in the flow. A few diameters downstream of the constriction, the flow

https://doi.org/10.1017/S0022112008002188 Published online by Cambridge University Press

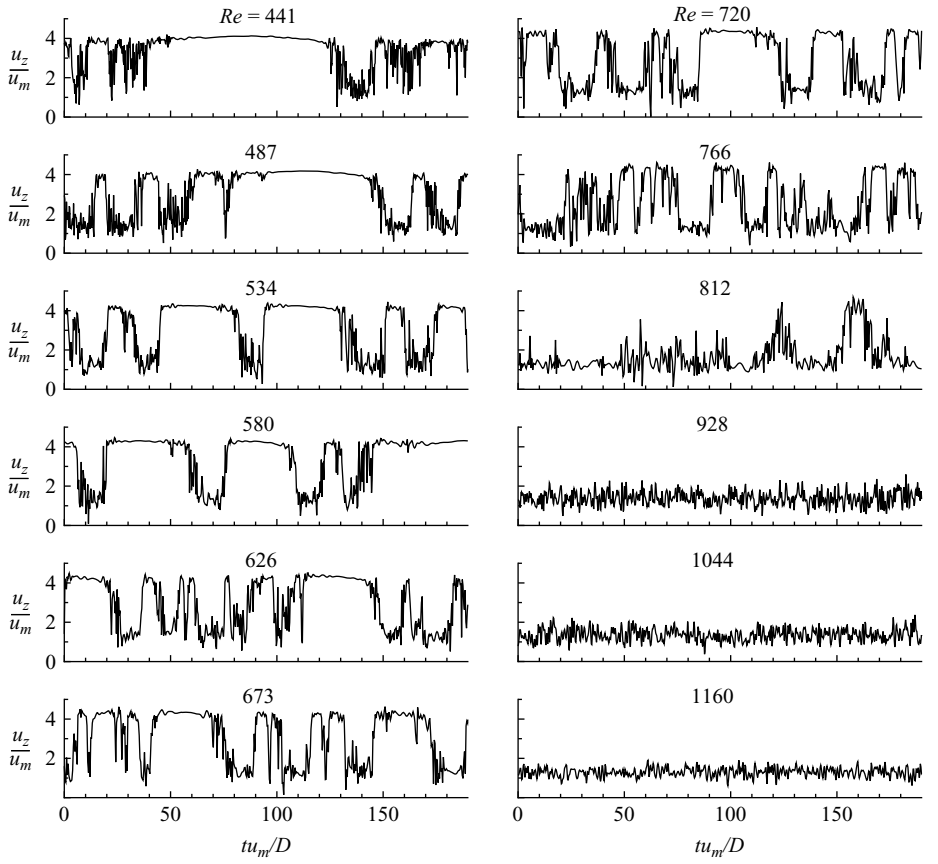

FIGURE 21. Time signals of the streamwise velocity extracted at $z/D = 7.5$ and $r/D = 0$ as a function of the Reynolds number.

oscillations are essentially induced by the periodic discharge of the separated region. In this case, the cyclic axial movement in the location of the turbulent breakdown is well located so that the time traces show a remarkable regularity, as observed by Sreenivasan & Strykowski (1983). Further downstream, the time series are still subject to this process and also to the fact that transition to turbulence can occur at varying axial locations. This phenomenon can be observed even if the flow immediately beyond the constriction is stable. Moreover, for moderate Reynolds numbers, a local flow relaminarization could potentially arise. Therefore, for several diameters downstream of the constriction, the regularity of the velocity–time signals is broken, and the apparent localized transitions between the different flow regimes could explain the flow irregularity observed in sudden expansion pipe flows by Iribarne *et al.* (1972), or the non-periodic unsteadiness and the violent fluctuations of the position of the reattachment point in the experiments of Latornell & Pollard (1986).

For a similar geometry, Ahmed & Giddens (1983*b*) observed a steady laminar flow regime at $Re = 250$, as also observed here since the time dependence arises for $Re \approx 400$, but a slight asymmetry is present in our study. They reported the occurrence of periodic oscillations for $Re = 500$ and observed turbulence at $Re = 1000$, in agreement with the transient and stationary data observed in figure 21. In the work of Sherwin & Blackburn (2005), the asymptotic state of the flow at $Re = 750$ showed a

https://doi.org/10.1017/S0022112008002188 Published online by Cambridge University Press

cyclic axial motion of the location where turbulent breakdown occurred with a period of $\Delta t u_m/D \sim 35$, associated with a slow flapping of the internal jet. These long-period fluctuations are of the same order of magnitude as the axial flow oscillations reported here. The flapping can also be compared to the slow swirling motion of the jet, which is constrained to deflect towards the wall in a certain azimuthal angle range due to small geometrical imperfections, obviously absent in the simulations. The linear instability theory applied by Sherwin & Blackburn (2005) predicted a critical Reynolds number $Re_c \approx 700$ whereas here we have $Re_c \approx 400$. In our study, the appearance of large-scale oscillations is observed gradually. For the smallest Reynolds numbers, laminar flow phases can persist over a time period as long as $200D/u_m$ and are very irregular. The phenomenon becomes more regular with the increase of Re and disappears for $Re \approx 900$ where a stationary turbulent state is observed. Since the DNS results of Sherwin & Blackburn (2005) are not available in this Reynolds number range, the discrepancies cannot be explained from physical aspects. However, in their linear stability analysis, the velocity was decomposed into an unstable steady base flow and a perturbation flow. The base flow chosen was axisymmetric (two-dimensional) and two-component, and the resulting three-dimensional instability was used to form the small perturbation flow component leading to transition to turbulence in direct numerical simulations. Our results indicate that in the presence of small geometric imperfections, a stable asymmetric solution for low Reynolds numbers is obtained. Thus, it would be of interest to perform a numerical perturbation analysis to obtain an asymmetric solution, followed by a stability analysis of this asymmetric base flow for comparison with present results. In numerical simulations, the occurrence of unsteady fluctuations perturbed the flow sufficiently to observe the development of a Coanda-type wall attachment. Therefore, in the unsteady case, available numerical simulations and our measurements are in excellent agreement.

6.2. *Stationary flow*

In view of the apparent absence of square form oscillations in figure 21 for the maximum values of the Reynolds numbers, a full characterization of the flow was conducted at $Re = 1160$. This constitutes the subject of the study for the remainder of the paper. Figure 22 presents time-averaged properties of the flow past the constriction. The three-dimensional perspective plot of the streamwise velocity obtained at different cross-sections using stereoscopic measurements indicates that on average the flow is axisymmetric. This allows the study of the mean properties in an arbitrary meridional plane using two-dimensional measurements as shown in the other plots. The continuous plot of $\bar{u}_z$ shows that the velocity profile loses its parabolic shape downstream of the stenosis and tends towards the fully developed turbulent flow profile further downstream (see at $z/D = 6$). The centreline mean velocity decreases with axial distance from $4.75u_m$ at $z/D = 0$ to reach a constant value of $1.27u_m$ at $6D$. The turbulent intensity based on the in-plane velocity components u'_z and u'_r allows the shear layer separating in the divergent part of the constriction to be identified. Velocity fluctuations gradually increase at $r/D = \pm 0.25$ with the axial location and reach a maximum at $z/D \approx 3$. Downstream, the end of the potential core is marked by more uniform velocity fluctuation levels which decrease with z/D. The correlation $\overline{u'_z u'_r}$ non-dimensionalized by u_m^2, also plotted in figure 22, indicates that the maximum of the turbulent shear stress coincides approximately with the axial location of the end of the potential core and is reached at two symmetric extrema in the meridional plane. However, the Reynolds shear stress rapidly falls downstream. Finally, the mean azimuthal vorticity $\bar{\omega}_\theta$ clearly highlights the axisymmetric shear layer by the two

https://doi.org/10.1017/S0022112008002188 Published online by Cambridge University Press

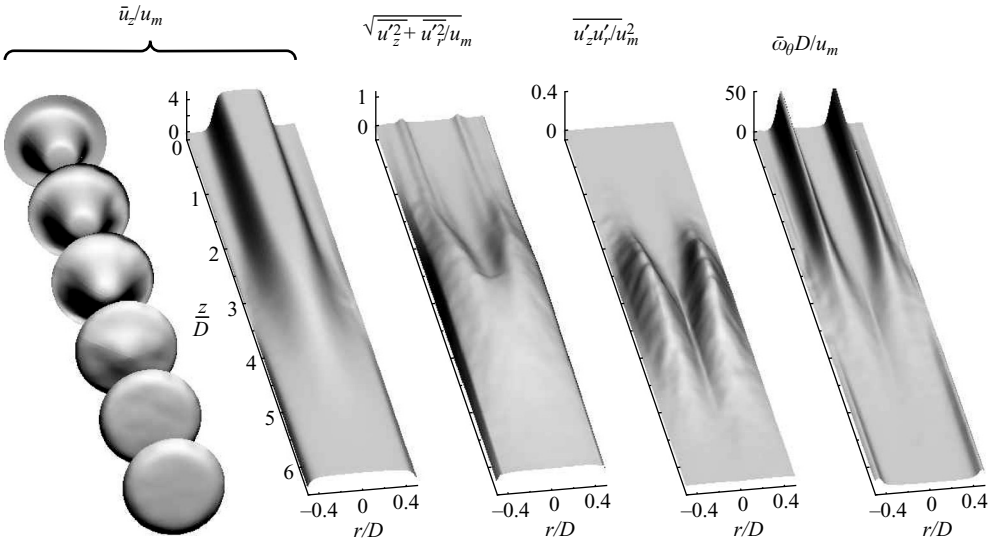

FIGURE 22. Time-averaged flow characteristics for $Re = 1160$.

symmetric vorticity peaks immediately downstream of the constriction, followed by a decrease with the streamwise coordinate to reach zero for maximum values of z/D except in the boundary layer close to the pipe wall. These results show that for the present Reynolds number ($Re = 1160$), the flow is axisymmetric and its behaviour can be related to the flow properties of a confined turbulent jet. A first region is observed in the vicinity of the constriction exit ($z/D \leqslant 2$) in which the jet velocity distribution develops a nearly constant shape. As a consequence of the separation in the constriction, an axisymmetric region is established downstream and reaches a length of approximately $3.5D$. The jet–wall interaction constitutes the second region; here maximum velocity fluctuations are observed, followed by the flow redevelopment. This third region appears for $z/D \geqslant 6$ and is typical of self-preserving turbulent pipe flow. Further downstream, the flow relaminarizes and recovers its characteristic parabolic profile but the distance required to achieve fully developed Poiseuille flow is much longer than is available in the present experiments.

At $Re = 1000$, Ahmed & Giddens (1983*a*) localized turbulent breakdown at $z/D \approx 2$, which coincides here with the end of the potential core. Their time-averaged statistics at $Re = 2000$ can be scaled to assess the present results obtained at our maximum Reynolds number of $Re = 1160$. Good agreement is obtained on the mean streamwise velocity distribution throughout the poststenotic region. Their fully developed turbulent profile is reached at $z/D = 5$, which is consistent with our data. Comparisons of mean squared values shows qualitative and quantitative agreement.

Figure 22 shows that the average streamwise velocity is correctly estimated in the meridional plane but the second-order moments seem less accurate. This is especially visible in the scatter of the shear stress data. Usually calculations of the cross-correlations are less sensitive to noise compared to estimation of the mean square values (Antonia 1972). However, time-averaged statistics has been obtained with ensemble averages of approximately 10 000 instantaneous velocity vector fields. An explanation may be found in the results presented in figure 23. Two instantaneous velocity vector fields and their spanwise vorticity map are shown in a meridional plane downstream of the stenosis. The velocity vectors are plotted in a frame of

https://doi.org/10.1017/S0022112008002188 Published online by Cambridge University Press

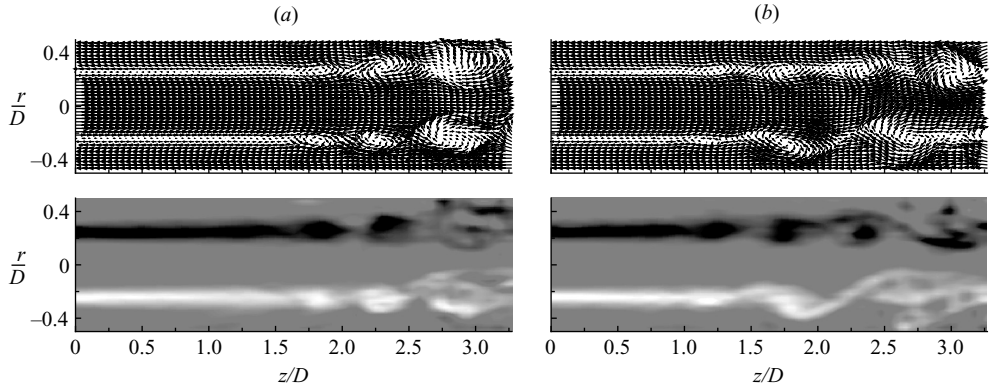

FIGURE 23. Instantaneous velocity vector fields and associated spanwise vorticity for $Re = 1160$: (a) symmetric and (b) non-symmetric cases. A constant velocity of $u_c = 2u_m$ has been subtracted to the streamwise velocity component.

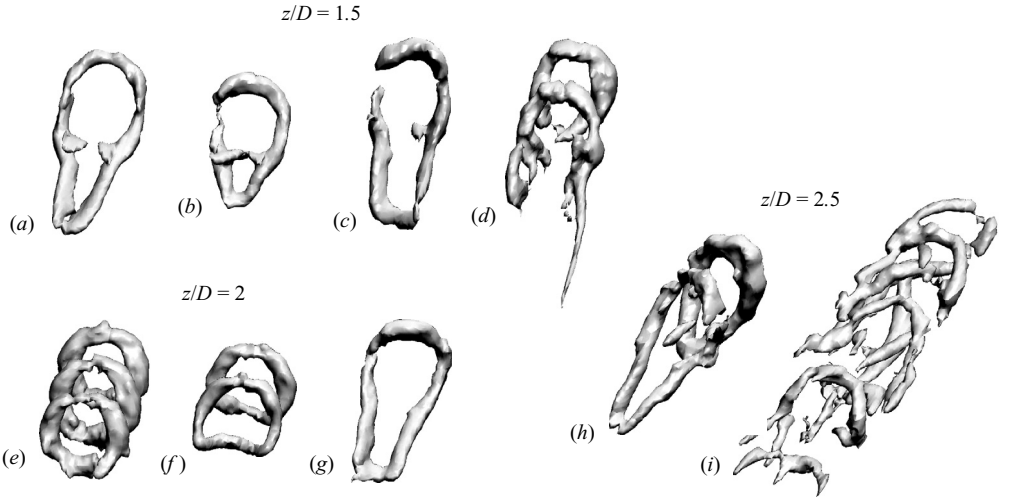

FIGURE 24. Selection of vortical structures obtained for $Re = 1160$: (a–d) hairpin-like vortices extracted at $z/D = 1.5$; (e, f) vortex rings and (g) hairpin vortex extracted at $z/D = 2$; (h, i) distorted patterns extracted at $z/D = 2.5$.

reference convected at $u_c = 2u_m$. Figure 23(a) presents a typical data set obtained when the flow develops symmetrically with respect to the pipe axis. The growing disturbance with the axial location is easily seen in the form of the three consecutive vortex pairs of increasing sizes, indicating that vortex rings are forming downstream of the constriction. In the plot in figure 23(b), the unsteady flow is asymmetric with disturbances growing to form flow patterns which are shed alternately from the top and bottom walls of the pipe, as indicated by the spanwise vorticity. In the case of the asymmetric flow pattern the eddy formation is observed at an axial location closer to the stenosis outflow section than that in the case of the formation of symmetric vortex rings. Hence, these two different vortex shedding scenarios will affect time-averaged flow properties.

The Taylor hypothesis was used again to identify vortical structures. Figure 24 presents a selection of vortices defined by isosurfaces of λ_{ci} adapted to each pattern

https://doi.org/10.1017/S0022112008002188 Published online by Cambridge University Press

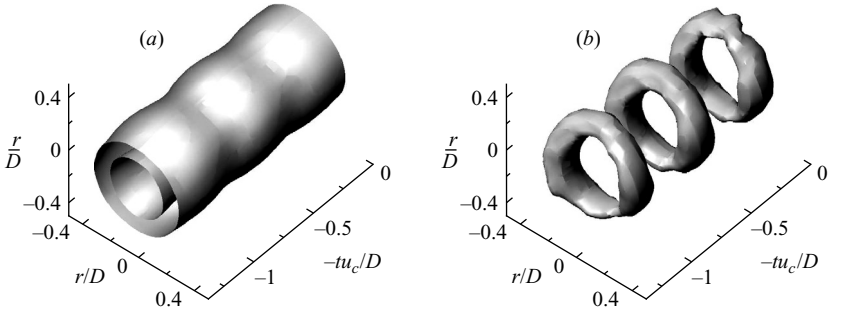

FIGURE 25. Vortex identification based on the Taylor hypothesis applied to linear stochastic estimates of velocity vectors at $z/D = 2$ for $Re = 1160$: (*a*) isosurface of $|\boldsymbol{\omega}|$ with 50 % of maximum and (*b*) isosurface of $\lambda_{ci} = 2.5$.

for visual convenience. All structures obtained at $z/D = 1.5$ are non-symmetric. This is not surprising because in the case of a symmetric instantaneous flow picture, the vortex formation is delayed downstream (cf. figure 23). The vortical structures presented fall in the category of hairpin-like vortices of varying sizes (figure 24*a* and 24*b*) and degree of asymmetry (figure 24*c*). The pattern of figure 24(*d*) is typical of two consecutive Ω-shaped structures, with a long leg on the upstream vortex. For the location of $z/D = 2$, three vortex rings are clearly seen in figure 24(*e*) and appear more distorted in the tilted structures of figure 24(*f*). Figure 24(*g*) shows that hairpin vortex can also occur at this axial location. Finally, the last plots obtained at $z/D = 2.5$ show highly distorted patterns. The basic flow structure in figure 24(*h*) highlights again the presence of a hairpin-like structure but most of the results obtained at this axial location are similar to the highly distorted pattern of figure 24(*i*), which qualitatively indicates that the flow structure evolves towards turbulence rapidly with the axial direction. Further downstream, isosurfaces of λ_{ci} are highly deformed and vortex structure identification is problematic.

To identify the dominant flow eddies at $Re = 1160$ and to provide a basis for physical interpretation, the linear stochastic estimation technique (Adrian & Moin 1988), based on the one-point, second-order space–time correlation tensor, was applied to our stereoscopic measurements. The reference point was chosen in a radial coordinate close to a position of highest velocity fluctuation amplitudes, and the Taylor hypothesis and vortex identification technique were used in a similar manner as previously explained. Figure 25(*a*) shows vorticity isosurfaces corresponding to half the maximum of $|\boldsymbol{\omega}|$. Iso-surfaces are almost entirely composed of azimuthal vorticity and reflect the shear-layer development downstream of the constriction. Identification of the vortices by the λ_{ci} isosurface in figure 25(*b*) clearly demonstrates the predominance of vortex rings at this axial location. Three complete patterns are entirely described, which highlights the high degree of coherence of the structures identified. The final conclusion which can be drawn from these results is that the vortex rings, occurring with sufficient strength to leave an imprint on the flow statistics (Christensen & Adrian 2001), are the dominant flow structures.

7. Conclusions

The structure of the flow past a smooth axisymmetric constriction has been described in detail via velocity measurements. Upstream and downstream pipe sections made of clear transparent material were inserted in a specially designed

https://doi.org/10.1017/S0022112008002188 Published online by Cambridge University Press

tank to use stereoscopic particle image velocimetry. After verifying that the flow exhibits the expected fully developed Poiseuille profile at the constriction entrance, velocity measurements indicated an asymmetric distribution of the streamwise velocity in cross-sectional planes when the Reynolds number Re, based on the upstream flow conditions, reaches a value of a few hundred, while the flow remains steady. The internal laminar jet which separates in the diverging part of the constriction is deflected towards the pipe wall in a preferred direction as a consequence of a Coanda-type wall attachment. Two-dimensional velocity measurements, obtained in the meridional plane of symmetry, show that the recirculation region is confined on one side of the wall and that the asymmetry is weak compared to the case of planar sudden expansions. The symmetry-breaking bifurcation of two-dimensional channel flows has been extensively studied in the literature, but we found no experimental data on the same phenomenon for axisymmetric configurations, for which velocity-measurement mappings are more difficult to obtain. As a result, numerical research on symmetry-breaking bifurcations focused on two-dimensional channel geometries. The phenomenon was, however, predicted numerically by Sherwin & Blackburn (2005) in the unsteady phase of the flow.

With increasing values of the Reynolds number, the flow remains steady and the asymmetry becomes more pronounced. For $Re > Re_c$, where $Re_c \approx 400$ is the critical Reynolds number, the jet detaches from the wall and the flow becomes highly intermittent. The recirculation region is particularly unstable and subject to long-time oscillations between unsteady phases, in which the enclosed fluid is entrained in the main flow forming an unstable shear layer, and steady phases, in which more stabilizing conditions allow the regeneration of the separated region. The formation of a second recirculation region, downstream of the first one and at the opposite pipe wall, is also observed intermittently during the flow cycle. Further downstream, velocity fluctuations indicate turbulence breakdown so a probe placed at a fixed axial location will show time signal alternating phases of calm and disturbed events caused by the axial movement of the turbulent front. Sreenivasan & Strykowski (1983) also observed the two-level velocity traces in a sudden pipe expansion. They indicated an extraordinary sensitivity of the phenomenon to the inlet flow conditions, and particularly emphasized that, for visual inspection of the process, the dye-injecting needle should be placed upstream of the inlet pipe as in the original experiments of O. Reynolds. The turbulence breakdown has mainly been described, in both previous poststenotic and sudden expansion flow studies, by local dye visualizations. The extreme care needed to avoid oscillation damping probably explains why the phenomenon has not been further reported in the literature. It should also explain the discrepancies in reported values of the critical Reynolds number. Our unsteady flow characteristics were also observed numerically by the direct numerical simulations of Sherwin & Blackburn (2005), although the critical Reynolds numbers are different. However, our data suggest that the steady asymmetric flow obtained is a direct consequence of inherent geometrical imperfections of the experimental setup, which are obviously totally absent in the simulations. The asymmetric flow features which are captured numerically when the flow becomes unsteady, i.e. in presence of flow perturbations, support this explanation. Therefore, a more rigorous comparison could be made by analysing the stability of the asymmetric base flow obtained numerically from an imperfect geometry.

The characteristic flow oscillations gradually disappear with further increase of the Reynolds number. The instantaneous velocity fields show that the asymmetry is still present in the vortex formation but the flow recovers symmetry as far as the mean

https://doi.org/10.1017/S0022112008002188 Published online by Cambridge University Press

properties are concerned. The use of linear stochastic estimation illustrates that the unstable jet formed downstream of the constriction rapidly evolves towards vortex rings before breakdown to turbulence.

The discrete wavelet transform was also particularly useful for extracting midplane vortex signatures. Two-dimensional measurements provided a basis to validate the use of the Taylor hypothesis for reconstructing the three spatial dimensions from data history. A vortex identification criterion was then applied to frozen the vortex topology. Isosurfaces of λ_{ci} thresholds uncovered quasi-streamwise counter-rotating vortex pairs at the onset of instabilities, which transform into arches vortices. Finally, hairpin-like vortices with varying sizes and asymmetry appear.

The general process of vortex packet formation described here is very similar to that observed in the DNS study of Zhou *et al.* (1999). As evidence of hairpin vortex formation is found in the near-wall and the outer region of boundary layers, our observations confirm the mechanism proposed in the conceptual model of Adrian *et al.* (2000). This increases the likelihood that the hairpin vortex paradigm is a unifying concept for turbulent wall bounded flows.

The authors wish to thank J.-M. Béland for the technical support which allowed the stereoscopic measurements to be performed in the best-suited manner, and for his helpful care in the important preparation of the inlet flow conditions.

REFERENCES

Adrian, R. J., Meinhart, C. D. & Tomkins, C. D. 2000 Vortex organization in the outer region of the turbulent boundary layer. *J. Fluid Mech.* **422**, 1–54.

Adrian, R. J. & Moin, P. 1988 Stochastic estimation of organized turbulent structure: homogeneous shear flow. *J. Fluid Mech.* **190**, 531–559.

Ahmed, S. A. & Giddens, D. P. 1983*a* Velocity measurements in steady flow through axisymmetric stenoses at moderate Reynolds numbers. *J. Biomech.* **16**, 505–516.

Ahmed, S. A. & Giddens, D. P. 1983*b* Flow disturbance measurements through a constricted tube at moderate Reynolds numbers. *J. Biomech.* **16**, 955–963.

Antonia, R. A. 1972 Conditionally sampled measurements near the outer edge of a turbulent boundary layer. *J. Fluid Mech.* **56**, 1–18.

Back, L. H. & Roschke, E. J. 1972 Shear-layer flow regimes and wave instabilities and reattachment lengths downstream of an abrupt circular channel expansion. *J. Appl. Mech.* **39**, 677–681.

Berger, S. A. & Jou, L.-D. 2000 Flows in stenotic vessels. *Annu. Rev. Fluid Mech.* **32**, 347–384.

Bluestein, D., Gutierrez, C., Londono, M. & Schoephoerster, R. T. 1999 Vortex shedding in steady flow through a model of an arterial stenosis and its relevance to mural platelet deposition. *Ann. Biomed. Engng* **27**, 763–773.

Cassanova, R. A. & Giddens, D. P. 1978 Disorder distal to modeled stenoses in steady and pulsatile flow. *J. Biomech.* **11**, 441–453.

Christensen, K. T. & Adrian, R. J. 2001 Statistical evidence of hairpin vortex packets in wall turbulence. *J. Fluid Mech.* **431**, 433–443.

Clark, C. 1976*a* The fluid mechanics of aortic stenosis – I. Theory and steady flow experiments. *J. Biomech.* **9**, 521–528.

Clark, C. 1976*b* Turbulent velocity measurements in a model of aortic stenosis. *J. Biomech.* **9**, 677–687.

Deshpande, M. D. & Giddens, D. P. 1980 Turbulence measurements in a constricted tube. *J. Fluid Mech.* **97**, 65–89.

Deshpande, M. D., Giddens, D. P. & Mabon, R.F. 1976 Steady laminar flow through modeled vascular stenoses. *J. Biomech.* **9**, 165–174.

Farge, M. 1992 Wavelet transforms and their application to turbulence. *Annu. Rev. Fluid Mech.* **24**, 395–457.

https://doi.org/10.1017/S0022112008002188 Published online by Cambridge University Press

Fearn, R. M., Mullin, T. & Cliffe, K. A. 1990 Nonlinear flow phenomena in a symmetric sudden expansion. *J. Fluid Mech.* **211**, 595–608.

Feuerstein, I. A., Pike, G. K. & Round, G. F. 1975 Flow in an abrupt expansion as a model for biological mass transfer experiments. *J. Biomech.* **8**, 41–51.

Forrester, J. H. & Young, D. F. 1970*a* Flow through a converging–diverging tube and its implications in occlusive vascular disease – I. Theoretical development. *J. Biomech.* **3**, 297–305.

Forrester, J. H. & Young, D. F. 1970*b* Flow through a converging-diverging tube and its implications in occlusive vascular disease – II. Theoretical and experimental results and their implications. *J. Biomech.* **3**, 307–316.

Iribarne, A., Frantisak, F., Hummel, R. L. & Smith, J. W. 1972 An experimental study of instabilities and other flow properties of a laminar pipe jet. *AIChE J.* **18**, 689–698.

Kim, B. M. & Corcoran, W. H. 1974 Experimental measurements of turbulence spectra distal to stenoses. *J. Biomech.* **7**, 335–342.

Ku, D. N. 1997 Blood flow in arteries. *Annu. Rev. Fluid Mech.* **29**, 399–434.

Latornell, D. J. & Pollard, A. 1986 Some observations on the evolution of shear layer instabilities in laminar flow through axisymmetric sudden expansion. *Phys. Fluids* **29**, 2828–2835.

Lee, J. S. & Fung, Y. C. 1970 Flow in locally constricted tubes at low Reynolds numbers. *J. Appl. Mech.* **37**, 9–16.

Macagno, E. O. & Hung, T.-K. 1967 Computational and experimental study of a captive annular eddy. *J. Fluid Mech.* **28**, 43–64.

Monnet, P., Menard, C. & Sigli, D. 1982 Some new aspects of the slow flow of a viscous fluid through an axisymmetric duct expansion or contraction – II. Experimental part. *Appl. Sci. Res.* **39**, 233–248.

Prasad, A. K. 2000 Stereoscopic particle image velocimetry. *Exps. Fluids* **29**, 103–116.

Robinson, S. K. 1991 Coherent motions in the turbulent boundary layer. *Annu. Rev. Fluid Mech.* **23**, 601–639.

Sherwin, S. J. & Blackburn, H. M. 2005 Three-dimensional instabilities and transition of steady and pulsatile axisymmetric stenotic flows. *J. Fluid Mech.* **533**, 297–327.

Sreenivasan, K. R. & Strykowski, P. J. 1983 An instability associated with a sudden expansion in a pipe flow. *Phys. Fluids* **26**, 2766–2768.

Varghese, S. S. & Frankel, S. H. 2003 Numerical modeling of pulsatile turbulent flow in stenotic vessels. *J. Biomech. Engng* **125**, 445–460.

Varghese, S. S., Frankel, S. H. & Fischer, P. F. 2007 Direct numerical simulation of stenotic flows. Part1. Steady flow. *J. Fluid Mech.* **582**, 253–280.

Young, D. F. 1979 Fluid mechanics of arterial stenoses. *J. Biomech. Engng* **101**, 157–175.

Young, D. F. & Tsai, F. Y. 1973 Flow characteristics in models of arterial stenoses – I. Steady flow. *J. Biomech.* **6**, 395–410.

Zhou, J., Adrian, R. J., Balachandar, S. & Kendall, T. M. 1999 Mechanisms for generating coherent packets of hairpin vortices in channel flow. *J. Fluid Mech.* **387**, 353–396.

https://doi.org/10.1017/S0022112008002188 Published online by Cambridge University Press